Computer Methods in Applied Mechanics and Engineering 448 (2026) 118439

Contents lists available at ScienceDirect

Comput. Methods Appl. Mech. Engrg.

journal homepage: www.elsevier.com/locate/cma

Inverse scattering without phase: Carleman convexification and phase retrieval via the Wentzel–Kramers–Brillouin approximation

Thuy T. Le [a,*], Phuong M. Nguyen [b], Loc H. Nguyen [b]

[a] Department of Mathematics, NC State University, Raleigh, 27695, NC, USA
[b] Department of Mathematics and Statistics, University of North Carolina at Charlotte, Charlotte, 28223, NC, USA

ARTICLE INFO

Keywords:
Phaseless inverse scattering
Carleman convexification method
Phase retrieval
Fourier expansion
Numerical reconstruction

ABSTRACT

This paper addresses the challenging and interesting inverse problem of reconstructing the spatially varying dielectric constant of a medium from phaseless backscattering measurements generated by single-point illumination. The underlying mathematical model is governed by the three-dimensional Helmholtz equation, and the available data consist solely of the magnitude of the scattered wave field. To address the nonlinearity and servere ill-posedness of this phaseless inverse scattering problem, we introduce a robust, globally convergent numerical framework combining several key regularization strategies. Our method first employs a phase retrieval step based on the Wentzel–Kramers–Brillouin (WKB) ansatz, where the lost phase information is reconstructed by solving a nonlinear optimization problem. Subsequently, we implement a Fourier-based dimension reduction technique, transforming the original problem into a more stable system of elliptic equations with Cauchy boundary conditions. To solve this resulting system reliably, we apply the Carleman convexification approach, constructing a strictly convex weighted cost functional whose global minimizer provides an accurate approximation of the true solution. Numerical simulations using synthetic data with high noise levels demonstrate the effectiveness and robustness of the proposed method, confirming its capability to accurately recover both the geometric location and contrast of hidden scatterers.

1. Introduction

Inverse scattering problems, particularly those involving wave propagation through media with spatially varying dielectric properties, have broad applications in scientific and engineering disciplines. Consider a medium whose dielectric characteristics are represented by a smooth function $c : \mathbb{R}^3 \to [1, \infty)$. Let $\Omega = (-R, R)^3 \subset \mathbb{R}^3$, with $R > 0$, denote our region of interest. Throughout this study, we assume that the dielectric constant satisfies

$$c(\mathbf{x}) = \begin{cases} \geq 1, & \mathbf{x} \in \Omega, \\ = 1, & \mathbf{x} \in \mathbb{R}^3 \setminus \Omega, \end{cases} \tag{1}$$

which implies a vacuum-like medium surrounding Ω, and regions of higher dielectric values within Ω correspond to embedded scatterers. Practical examples of such scatterers include buried explosive devices, underground mineral deposits, tumors in biological tissues, defects within structural materials, and microscopic or nanoscopic inhomogeneities. These inverse scattering scenarios are fundamental to many areas, such as remote sensing, non-destructive evaluation, medical imaging, and materials science.

* Corresponding author.
E-mail addresses: tle9@ncsu.edu (T.T. Le), pnguye45@charlotte.edu (P.M. Nguyen), loc.nguyen@charlotte.edu (L.H. Nguyen).

https://doi.org/10.1016/j.cma.2025.118439
Received 21 April 2025; Received in revised form 24 September 2025; Accepted 25 September 2025
Available online 9 October 2025

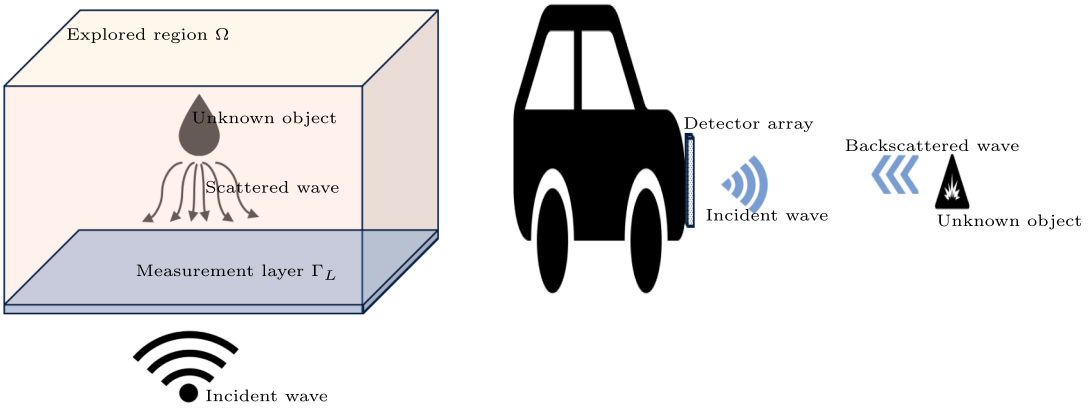

(a) Schematic illustration of inverse scattering

(b) Remote sensing example

Fig. 1. (a) Illustration of the inverse scattering scenario, showing incident waves interacting with an unknown object in an inaccessible region Ω, producing scattered waves measured on the observation layer Γ_L. (b) Real-world example demonstrating remote detection of hidden objects using reflected wave data collected by a detector array.

To remotely detect and characterize scatterers, one illuminates the domain Ω with an incident wave originating from a single point source located at $\mathbf{x}_0 = (0, 0, -d) \notin \Omega$, where $d > R$. This wave interacts with scatterers inside Ω, creating scattered waves that radiate outward. We measure only the magnitude (intensity) of the resulting scattered wave field on a three-dimensional measurement layer

$$\Gamma_L = (-R, R)^2 \times (-R, -R + L),$$

located immediately at the bottom of the domain Ω, with some thickness $L > 0$. Fig. 1 provides both schematic and practical visualizations of this measurement scenario. The central goal of our phaseless inverse scattering problem is to reconstruct the dielectric function $c(\mathbf{x})$ using these intensity-only measurements, thereby revealing the position, shape, and dielectric contrasts of the hidden scatterers.

Phaseless inverse scattering problems naturally arise in applications where the phase measurement is difficult or infeasible, such as in high-frequency regimes with rapid oscillations that preclude accurate phase detection. In contrast to conventional inverse scattering problems, where both amplitude and phase are typically available, phaseless measurements lead to greater mathematical complexity due to increased nonlinearity and limited data. As a consequence, it is generally necessary to collect intensity data over a three-dimensional measurement volume rather than on a simpler two-dimensional boundary surface.

The theoretical and practical significance of phaseless inverse scattering has long been recognized. A classical question posed by Chadan and Sabatier [1, Chapter 10] "*How can inverse scattering problems be solved using only magnitude data?*" has driven extensive research. Early theoretical investigations, such as uniqueness results for the one-dimensional Schrödinger equation [2,3], laid foundational understanding. Subsequently, these uniqueness results have been extended to multi-dimensional Schrödinger and Helmholtz equations under various assumptions [4–8].

While analytic reconstruction methods have been proposed [9–12], these methods often require measurements across a wide frequency spectrum, limiting their practicality. More computationally feasible numerical approaches for realistic frequency ranges have thus been developed, demonstrating successful reconstructions from simulated and experimental data [13–15]. Further numerical methods utilizing Kirchhoff migration and Born approximations have been studied in [16,17], and shape reconstruction from phaseless data has also received considerable attention [18–22]. Recently, the paper [23] introduced a weighted stabilized Lagrange interpolation collocation method for boundary condition identification in electromagnetic inverse scattering problems. This non-iterative method incorporates regularization techniques to handle noisy data, enhancing the accuracy of reconstruction. Additionally, the paper [24] presented a weighted radial basis collocation method for nonlinear inverse Helmholtz problems, which focuses on parameter identification with regularization and efficient numerical methods. Both methods contribute significantly to the field by emphasizing the role of regularization and efficient computational strategies to address challenges in inverse scattering and parameter identification.

In this paper, we investigate the phaseless inverse scattering problem under single-source illumination using multi-frequency data. While linearization-based methods can effectively localize scatterers, they often fail to accurately reconstruct high-contrast variations, see e.g. [15]. To address this limitation, we propose a novel, globally convergent reconstruction method that combines the Wentzel–Kramers–Brillouin (WKB) ansatz, a Fourier filtering technique, and the Carleman convexification approach. By entirely avoiding linearization, our method significantly improves reconstruction accuracy and robustness. Specifically, our proposed numerical framework consists of three interconnected components. First, we develop a robust phase retrieval procedure that leverages the WKB ansatz

and nonlinear optimization to accurately recover complex wave fields from phaseless measurements. Next, we apply a Fourier-based frequency reduction technique, transforming the original inverse problem into a stable elliptic system with Cauchy boundary conditions. Finally, the Carleman convexification method is employed to construct a weighted cost functional, ensuring strict convexity and enabling stable global minimization. Numerical experiments clearly illustrate that our approach effectively recovers both the location and high contrast of scatterers, even in the presence of noise.

While the Fourier-based dimension reduction technique and Carleman convexification approach are well-established methods, the novelty of this work lies in how we combine and extend these methods to solve the phaseless inverse scattering problem in a more robust and generalizable way. A key new contribution of this paper is the use of the Wentzel-Kramers-Brillouin (WKB) ansatz to recover the phase from phaseless data. This approach enables us to reconstruct phase information using nonlinear optimization, a significant advancement that enhances the accuracy and stability of the solution, particularly in noisy environments. Additionally, the Carleman convexification method employed here differs from its previous applications, such as in [25–27]. In those works, strong smoothness conditions were imposed on the noise to ensure stability. However, in this paper, we extend the work in [28] by including the integral on the measurement surface Γ when defining the cost functional $J_{\lambda,\epsilon}$ with a suitable Carleman weighted function. This modification relaxes the regularity condition on noise, making the method more realistic where noise may not be smooth. By combining the WKB ansatz for phase retrieval with the improved Carleman convexification method, this paper presents a globally convergent and computationally efficient framework for solving the phaseless inverse scattering problem. These innovations, particularly in handling noisy and phaseless data, represent a significant advancement over conventional methods.

The structure of the paper is as follows. Section 2 introduces the problem formulation together with the WKB-based phase retrieval procedure. Section 3 presents the frequency dimension reduction method, while Section 4 develops the Carleman convexification framework and its convexity analysis. Section 5 reports numerical simulations that validate the proposed approach. Additional analysis of the algorithm is discussed in Section 6, and concluding remarks are given in Section 7.

2. Problem statement and phase reconstruction via the Wentzel–Kramers–Brillouin ansatz

Consider an inverse scattering scenario governed by the Helmholtz equation in three-dimensional space. Let $[\underline{k}, \overline{k}]$ denote an interval of wave numbers and $\mathbf{x}_0 = (0, 0, -d)$, with $d > R$, represent a fixed point source outside the domain Ω. The incident wave generated by this source at wave number k is given explicitly by

$$u_{\text{inc}}(\mathbf{x}, k) = \frac{e^{\mathrm{i}k|\mathbf{x}-\mathbf{x}_0|}}{4\pi|\mathbf{x}-\mathbf{x}_0|}, \quad (\mathbf{x}, k) \in \mathbb{R}^3 \times [\underline{k}, \overline{k}]. \tag{2}$$

When this incident wave interacts with the scatterers embedded in the domain Ω, characterized by the spatially varying dielectric constant $c(\mathbf{x})$, it generates the total wave field $u(\mathbf{x}, k)$, which satisfies the following problem:

$$\begin{cases} \Delta u + k^2 c(\mathbf{x}) u = 0, & \mathbf{x} \in \mathbb{R}^3, \\ \partial_{|\mathbf{x}|} u_{\text{sc}} - \mathrm{i}k u_{\text{sc}} = o(|\mathbf{x}|^{-1}), & |\mathbf{x}| \to \infty, \end{cases} \tag{3}$$

where the scattered wave u_{sc} is defined as the difference between the total and incident waves, i.e.,

$$u_{\text{sc}}(\mathbf{x}, k) = u(\mathbf{x}, k) - u_{\text{inc}}(\mathbf{x}, k), \quad (\mathbf{x}, k) \in \mathbb{R}^3 \times [\underline{k}, \overline{k}]. \tag{4}$$

In many practical situations, only the intensity (modulus) of the wave can be measured. Thus, we consider the following inverse problem:

Problem 2.1 (Inverse scattering without phase information)**.** Given the phaseless measurements

$$f(\mathbf{x}, k) = |u(\mathbf{x}, k)|, \quad (\mathbf{x}, k) \in \Gamma_L \times [\underline{k}, \overline{k}], \tag{5}$$

reconstruct the dielectric constant $c(\mathbf{x})$ within the domain Ω.

Addressing this phaseless inverse scattering problem presents significant challenges due to its inherent nonlinearity and ill-posedness. To reconstruct the lost phase information, we use the classical WKB ansatz, which approximates the wave field:

$$u(\mathbf{x}, k) = A(\mathbf{x}) e^{ik\tau(\mathbf{x})} + \mathcal{O}(1/k) \quad \text{as } k \to \infty \tag{6}$$

for some positive functions A and τ.

This asymptotic form is well-established in the literature. For the stationary Schrödinger equation, its validity under the Born approximation has been demonstrated in foundational studies such as [29–31], and analogous reasoning extends naturally to the Helmholtz equation. Beyond the Born approximation, the first rigorous justification was presented in [32, Theorem 17], with a more refined analysis appearing much later in [11]. For clarity, we summarize below the key conditions provided in [11] under which the ansatz is valid:

1. The coefficient $c(\mathbf{x})$ is assumed to belong to the class C^{15}.
2. For every $\mathbf{x} \in \Omega$, there exists a unique geodesic line connecting the source $\mathbf{x}_0$ and $\mathbf{x}$ with respect to the Riemannian metric $\sqrt{c(\mathbf{x})}|d\mathbf{x}|$, where $|d\mathbf{x}| = \sqrt{dx^2 + dy^2 + dz^2}$.

Although these conditions rigorously justify the WKB ansatz Eq. (6), they may not be practical to verify for finite k or in real-world applications. Therefore, we adopt the ansatz heuristically as a physically informed starting point for phase reconstruction. To estimate τ, we differentiate the ansatz, neglecting the $\mathcal{O}(1/k)$ term:

$$\nabla u(\mathbf{x},k) = (\nabla A(\mathbf{x}) + ik\nabla\tau(\mathbf{x}))e^{ik\tau(\mathbf{x})},$$
$$\Delta u(\mathbf{x},k) = \left(\Delta A(\mathbf{x}) + 2ik\nabla A(\mathbf{x})\cdot\nabla\tau(\mathbf{x}) + ikA(\mathbf{x})\Delta\tau(\mathbf{x}) - k^2A(\mathbf{x})|\nabla\tau(\mathbf{x})|^2\right)e^{ik\tau(\mathbf{x})}.$$

Substituting into the Helmholtz equation, we obtain:

$$\Delta u(\mathbf{x},k) + k^2c(\mathbf{x})u(\mathbf{x},k) = \left(\Delta A(\mathbf{x}) + 2ik\nabla A(\mathbf{x})\cdot\nabla\tau(\mathbf{x}) + ikA(\mathbf{x})\Delta\tau(\mathbf{x}) - k^2A(\mathbf{x})|\nabla\tau|^2 + k^2c(\mathbf{x})A(\mathbf{x})\right)e^{ik\tau(\mathbf{x})} = 0, \tag{7}$$

for all $(\mathbf{x},k)\in\Gamma_L\times[\underline{k},\overline{k}]$. In the high-frequency limit, the leading-order term,

$$-k^2A(\mathbf{x})|\nabla\tau|^2 + k^2c(\mathbf{x})A(\mathbf{x}),$$

must vanish, which yields the eikonal equation:

$$|\nabla\tau|^2 = c(\mathbf{x}) = 1 \quad \text{for } \mathbf{x}\in\Gamma_L, \tag{8}$$

using the assumption $c=1$ in $(\mathbb{R}^3\setminus\Omega)\cup\Gamma_L$.

Remark 1. Alternatively, the eikonal equation can be heuristically derived by viewing Eq. (7) as a quadratic equation in k. Enforcing that the equation holds for all k implies that the coefficient of the dominant term (and the other two lower order terms) must vanish, once again yielding Eq. (8).

Since τ denotes the travel time from $\mathbf{x}_0$ to $\mathbf{x}$, the natural choice of solution to Eq. (8) is:

$$\tau(\mathbf{x}) = |\mathbf{x}-\mathbf{x}_0| \quad \text{for all } \mathbf{x}\in\Gamma_L. \tag{9}$$

Using this phase, we define the initial guess:

$$u^{(0)}(\mathbf{x},k) = f(\mathbf{x},k)e^{ik|\mathbf{x}-\mathbf{x}_0|} \quad \text{for all } \mathbf{x}\in\Gamma_L, \quad k\in[\underline{k},\overline{k}], \tag{10}$$

as an approximation to the true wave field $u(\mathbf{x},k)$.

The ansatz Eq. (6) provides a mathematically grounded approximation of wave fields in the high-frequency regime. However, the constructed initial guess $u^{(0)}(\mathbf{x},k)$ may not exactly satisfy the Helmholtz equation, nor perfectly match the observed modulus data due to noise. To refine this estimate, we compute an improved approximation $u_{\text{phase}}(\mathbf{x},k)$ by minimizing the deviation from both the Helmholtz operator and the intensity constraint using appropriate balancing coefficients. Specifically, for each $k\in[\underline{k},\overline{k}]$, we solve the following variational problem:

$$J_k(v) = \frac{1}{k^4\|f(\cdot,k)\|^2_{L^2(\Gamma_L)}}\left\|\Delta v + k^2v\right\|^2_{L^2(\Gamma_L)} + \frac{1}{\|f(\cdot,k)\|^4_{L^2(\Gamma_L)}}\left\||v|^2 - f^2(\cdot,k)\right\|^2_{L^2(\Gamma_L)}, \tag{11}$$

where the minimization is over $v\in H^2(\Gamma_L)$. Among the local minimizers, we select the one closest to $u^{(0)}(\mathbf{x},k)$, and denote it by $u_{\text{phase}}(\mathbf{x},k)$. The functional $J_k(v)$ in Eq. (11) captures two complementary objectives: adherence to the PDE model in Γ_L, and conformity with the observed intensity. The first term, $\frac{1}{k^4\|f(\cdot,k)\|^2_{L^2(\Gamma_L)}}\|\Delta v + k^2v\|^2_{L^2(\Gamma_L)}$, penalizes deviation from the Helmholtz equation, while the second term, $\frac{1}{\|f(\cdot,k)\|^4_{L^2(\Gamma_L)}}\||v|^2 - f^2(\mathbf{x},k)\|^2_{L^2(\Gamma_L)}$, ensures alignment with the modulus data.

We introduced the scaling factors in Eq. (11) to balance the two terms in the cost functional. The dimension of the term $\|\Delta v + k^2v\|^2_{L^2(\Gamma_L)}$ is that of $k^4\|v\|^2_{L^2(\Gamma_L)} = k^4\|f(\cdot,k)\|^2_{L^2(\Gamma_L)}$, while the dimension of the term $\left\||v|^2 - f^2(\cdot,k)\right\|^2_{L^2(\Gamma_L)}$ is that of $\|f(\cdot,k)\|^4_{L^2(\Gamma_L)}$. Therefore, this scaling ensures that both terms in Eq. (11) are dimensionless and of comparable magnitude. In other words, introducing the scaling makes both terms contribute more evenly to the optimization process. This dual-objective formulation is standard and widely used in scientific and engineering communities. Restricting to the Sobolev space $H^2(\Gamma_L)$ ensures well-posedness and the necessary regularity to evaluate Laplacians and traces. This framework is particularly advantageous for mitigating the ill-posedness introduced by noise in the measured data. Initializing the optimization at $u^{(0)}$, which incorporates travel-time-informed phase information, increases the likelihood of convergence to a physically relevant solution in this non-convex landscape.

Remark 2. In the cost functional Eq. (11), we require the function v to belong to the Sobolev space $H^2(\Omega)$. This regularity assumption is standard in the inverse scattering literature and can be theoretically justified by assuming sufficient smoothness of the coefficient function $c(\mathbf{x})$, which ensures that the total field u also belongs to $H^2(\Omega)$. This is rigorously discussed, for example, via the Lippmann–Schwinger representation in [33, Chapter 8]. It is important to note, however, that this smoothness assumption on c is mainly introduced for the sake of theoretical analysis. In our numerical implementation (Section 5), we do not enforce any explicit smoothness on c, and the method still performs well. Moreover, requiring $v\in H^2(\Omega)$ has practical benefits: it promotes smoother reconstructions, which helps suppress high-frequency oscillations introduced by measurement noise. In this way, the H^2 regularity assumption also acts as an implicit regularization, reducing the nonsmoothness of the noise and contributing to a more stable numerical inversion.

Observe that $\Gamma_L \subset \Omega$, and its bottom boundary coincides with:

$$\Gamma = (-R, R)^2 \times \{z = -R\}, \tag{12}$$

which corresponds to the lower face of $\partial\Omega$. Thus, both u_{phase} and its normal derivative $\partial_z u_{\text{phase}}$ can be extracted on Γ, enabling the reformulation of the original phaseless inverse problem as follows:

Problem 2.2 (The inverse scattering problem with phase information)**.** *Given the functions*

$$g(\mathbf{x}, k) = u(\mathbf{x}, k) \quad \textit{and} \quad h(\mathbf{x}, k) = \partial_z u(\mathbf{x}, k) \tag{13}$$

for all $\mathbf{x} \in \Gamma \times [\underline{k}, \overline{k}]$*, reconstruct* $c(\mathbf{x})$ *for all* $\mathbf{x} \in \Omega$*.*

This formulation pertains to the phased inverse scattering problem, where both the modulus and phase of the backscattered wave are known on the measurement surface. Our research group has developed two distinct approaches, both leveraging Carleman estimates, to address this problem:

1. The Carleman convexification method [25–27,34];
2. The Carleman contraction mapping method [35].

The first step common to both methods is to reformulate Problem 2.2 as a nonlinear elliptic system of the form

$$\begin{cases} \Delta \mathbf{v} + \mathcal{L}_{\text{lin}}(\mathbf{v}, \nabla \mathbf{v}) + \mathcal{N}_{\text{nonlin}}(\mathbf{v}, \nabla \mathbf{v}) = 0 \text{ in } \Omega, \\ \text{subject to Cauchy boundary data,} \end{cases} \tag{14}$$

where $\mathbf{v}$ is a vector whose components are the Fourier coefficients of a transformed version of the wave field u (see Eq. (15)). The operators $\mathcal{L}_{\text{lin}}$ and $\mathcal{N}_{\text{nonlin}}$ are explicitly defined linear and nonlinear terms, respectively.

1. The Carleman convexification method computes $\mathbf{v}$ by minimizing a Carleman-weighted least-squares functional:

$$\varphi \mapsto \int_\Omega W(\mathbf{x}) \left| \Delta\varphi + \mathcal{L}_{\text{lin}}(\varphi, \nabla\varphi) + \mathcal{N}_{\text{nonlin}}(\varphi, \nabla\varphi) \right|^2 d\mathbf{x} + \text{regularization},$$

   subject to the prescribed Cauchy data in Eq. (14). The weight function $W(\mathbf{x})$ is chosen based on Carleman estimates to ensure strict convexity of the functional in appropriate bounded subsets of Sobolev spaces. This convexity ensures the uniqueness of the minimizer and allows for numerical computation using gradient-based optimization methods. For more on the construction of W and theoretical justifications, see [25–27,34].
2. The Carleman contraction mapping method approaches the solution of Eq. (14) by defining a map Φ as follows:

$$\mathbf{u} \mapsto \arg\min_{\varphi} \int_\Omega W(\mathbf{x}) \left| \Delta\varphi + \mathcal{L}_{\text{lin}}(\varphi, \nabla\varphi) + \mathcal{N}_{\text{nonlin}}(\mathbf{u}, \nabla\mathbf{u}) \right|^2 d\mathbf{x} + \text{regularization},$$

   where φ is required to satisfy the given Cauchy boundary conditions in Eq. (14). With an appropriately chosen Carleman weight function $W(\mathbf{x})$, the mapping Φ becomes a contraction, and its fixed point yields the solution to the original system. The theoretical foundation and convergence analysis for general equations of the form Eq. (14) can be found in [36,37], while the application of this method to the specific inverse scattering problem considered in this work is detailed in [35].

In this work, we adopt the first approach to solve the problem numerically. The primary motivation for this choice is that the Carleman convexification method has been validated with both simulated and experimental datasets. The contraction mapping method will be applied in future research.

3. The frequency dimension reduction model

Following the phase retrieval procedure described in Section 2, Problem 2.1 is reduced to reconstructing the coefficient $c(\mathbf{x})$ from boundary measurements of $u(\mathbf{x}, k)$ and $\partial_z u(\mathbf{x}, k)$ on $\Gamma \times [\underline{k}, \overline{k}]$, as defined in Problem 2.2. This inverse scattering problem is highly ill-posed, meaning that even minor perturbations in the input data, such as measurement noise, can result in substantial reconstruction errors. To mitigate this instability, we employ a frequency filtering technique using Fourier truncation, which suppresses high-frequency oscillations in the data. This process yields a system of elliptic equations with Cauchy boundary conditions, which is notably more stable and amenable to numerical computation. The formulation of this system also naturally aligns Problem 2.2 with the framework of the Carleman convexification method.

3.1. The logarithmic transformation

For the reader's convenience, we provide an overview of the Fourier truncation procedure in this section. The process begins with an algebraic transformation, following the algorithmic approach developed in [26,27,34,38]. Specifically, for each $(\mathbf{x}, k) \in \Omega \times [\underline{k}, \overline{k}]$, we define the logarithmic transformation

$$v(\mathbf{x}, k) = \frac{1}{k^2} \log \frac{u(\mathbf{x}, k)}{u_{\text{inc}}(\mathbf{x}, k)}. \tag{15}$$

Remark 3. Although taking the logarithm of the complex-valued function $\frac{u(\mathbf{x},k)}{u_{\text{inc}}(\mathbf{x},k)}$ in Eq. (15) may initially appear problematic, it is well-defined based on the definition of the complex logarithm presented in [38, Section 4.2]. The WKB ansatz Eq. (6) further supports this definition by ensuring that $\frac{u(\mathbf{x},k)}{u_{\text{inc}}(\mathbf{x},k)}$ remains nonzero for all $(\mathbf{x},k)\in\Omega\times[\underline{k},\overline{k}]$. In numerical implementations, evaluating this logarithm is straightforward and poses no practical difficulties.

By standard rules in differentiation, we have for all $(\mathbf{x},k)\in\Omega\times[\underline{k},\overline{k}]$

$$\nabla v(\mathbf{x},k)=\frac{1}{k^2}\left[\frac{\nabla u(\mathbf{x},k)}{u(\mathbf{x},k)}-\frac{\nabla u_{\text{inc}}(\mathbf{x},k)}{u_{\text{inc}}(\mathbf{x},k)}\right],$$

and

$$\begin{aligned}\Delta v(\mathbf{x},k)&=\frac{1}{k^2}\left[\frac{\Delta u(\mathbf{x},k)}{u(\mathbf{x},k)}-\left(\frac{\nabla u(\mathbf{x},k)}{u(\mathbf{x},k)}\right)^2-\frac{\Delta u_{\text{inc}}(\mathbf{x},k)}{u_{\text{inc}}(\mathbf{x},k)}+\left(\frac{\nabla u_{\text{inc}}(\mathbf{x},k)}{u_{\text{inc}}(\mathbf{x},k)}\right)^2\right]\\&=\frac{1}{k^2}\left[k^2(1-c(\mathbf{x}))-\left(\frac{\nabla u(\mathbf{x},k)}{u(\mathbf{x},k)}-\frac{\nabla u_{\text{inc}}(\mathbf{x},k)}{u_{\text{inc}}(\mathbf{x},k)}\right)\cdot\left(\frac{\nabla u(\mathbf{x},k)}{u(\mathbf{x},k)}+\frac{\nabla u_{\text{inc}}(\mathbf{x},k)}{u_{\text{inc}}(\mathbf{x},k)}\right)\right]\\&=1-c(\mathbf{x})-\nabla v(\mathbf{x},k)\cdot\left(k^2\nabla v(\mathbf{x},k)+\frac{2\nabla u_{\text{inc}}(\mathbf{x},k)}{u_{\text{inc}}(\mathbf{x},k)}\right).\end{aligned}\tag{16}$$

By a direct algebra, using the explicit formula of u_{inc} in Eq. (2) gives

$$\frac{\nabla u_{\text{inc}}(\mathbf{x},k)}{u_{\text{inc}}(\mathbf{x},k)}=\left(\mathrm{i}k-\frac{1}{|\mathbf{x}-\mathbf{x}_0|}\right)\frac{\mathbf{x}-\mathbf{x}_0}{|\mathbf{x}-\mathbf{x}_0|},\quad(\mathbf{x},k)\in\Omega\times[\underline{k},\overline{k}].\tag{17}$$

Combining Eqs. (16) and (17) gives

$$\Delta v(\mathbf{x},k)+k^2[\nabla v(\mathbf{x},k)]^2+2\left(\mathrm{i}k-\frac{1}{|\mathbf{x}-\mathbf{x}_0|}\right)\nabla v(\mathbf{x},k)\cdot\frac{\mathbf{x}-\mathbf{x}_0}{|\mathbf{x}-\mathbf{x}_0|}=1-c(\mathbf{x})\tag{18}$$

for all $(\mathbf{x},k)\in\Omega\times[\underline{k},\overline{k}]$. To eliminate the unknown c, we differentiate Eq. (18) with respect to k to obtain

$$\Delta\partial_k v(\mathbf{x},k)+2k[\nabla v(\mathbf{x},k)]^2+2k^2\nabla v(\mathbf{x},k)\cdot\nabla\partial_k v(\mathbf{x},k)+2\left(\mathrm{i}k-\frac{1}{|\mathbf{x}-\mathbf{x}_0|}\right)\nabla\partial_k v(\mathbf{x},k)\cdot\frac{\mathbf{x}-\mathbf{x}_0}{|\mathbf{x}-\mathbf{x}_0|}+2\mathrm{i}\nabla v(\mathbf{x},k)\cdot\frac{\mathbf{x}-\mathbf{x}_0}{|\mathbf{x}-\mathbf{x}_0|}=0\tag{19}$$

for $\mathbf{x}\in\Omega$, $k\in[\underline{k},\overline{k}]$.

Solving Eq. (19) is challenging because it does not take the form of a standard partial differential equation, and a theoretical framework for it has not yet been developed. As a result, we approach this problem using a frequency dimension reduction technique.

3.2. The frequency dimension reduction using Fourier expansion

We next apply a "Fourier filter" to eliminate the high-frequency oscillatory components of the function v. This process involves truncating the Fourier expansion of v using the polynomial-exponential basis $\{\Psi_n\}_{n\geq1}$ of $L^2(\underline{k},\overline{k})$. This basis was originally constructed in [39] via the Gram-Schmidt orthonormalization of the complete system $\{\phi_n(k)=k^{n-1}e^k\}_{n\geq1}$ in $[\underline{k},\overline{k}]$. A higher-dimensional extension of this basis was later developed in [40]. The rationale behind this choice will be further discussed in Remark 7.

For $\mathbf{x}\in\Omega$, the Fourier expansion of v is approximated as

$$v(\mathbf{x},k)=\sum_{n=1}^{\infty}v_n(\mathbf{x})\Psi_n(k)\approx\sum_{n=1}^{N}v_n(\mathbf{x})\Psi_n(k)\tag{20}$$

where the cutoff number N will be chosen later by a trial-error procedure, and the Fourier coefficient v_n is given by

$$v_n(\mathbf{x})=\int_{\underline{k}}^{\overline{k}}v(\mathbf{x},k)\Psi_n(k)dk.\tag{21}$$

Remark 4. The truncation in Eq. (20) acts as a filtering step, effectively regularizing any noise in the measured data by completely removing the high-frequency oscillatory components of v. Additionally, it significantly reduces computational costs by eliminating the frequency dimension. Specifically, instead of computing the function $v:\Omega\times[\underline{k},\overline{k}]\to\mathbb{C}$, which involves $3+1$ dimensions, we compute a finite number N of Fourier coefficients $v_n:\Omega\to\mathbb{C}$, reducing the problem to only three dimensions.

Plugging the approximation Eq. (20) into Eq. (19) gives

$$\begin{aligned}&\sum_{n=1}^{N}\Delta v_n(\mathbf{x})\Psi_n'(k)+2k\left[\sum_{n=1}^{N}\nabla v_n(\mathbf{x})\Psi_n(k)\right]^2+2k^2\sum_{n=1}^{N}\nabla v_n(\mathbf{x})\Psi_n(k)\cdot\sum_{n=1}^{N}\nabla v_n(\mathbf{x})\Psi_n'(k)\\&+2\left(\mathrm{i}k-\frac{1}{|\mathbf{x}-\mathbf{x}_0|}\right)\sum_{n=1}^{N}\nabla v_n(\mathbf{x})\Psi_n'(k)\cdot\frac{\mathbf{x}-\mathbf{x}_0}{|\mathbf{x}-\mathbf{x}_0|}+2\mathrm{i}\sum_{n=1}^{N}\nabla v_n(\mathbf{x})\Psi_n(k)\cdot\frac{\mathbf{x}-\mathbf{x}_0}{|\mathbf{x}-\mathbf{x}_0|}=0\end{aligned}\tag{22}$$

for all $(\mathbf{x},k)\in\Omega\times[\underline{k},\overline{k}]$. For each $m\in\{1,2,\dots,N\}$, multiplying $\Psi_m(k)$ to both sides of Eq. (22) and integrating the resulting equation, we obtain

$$\sum_{n=1}^{N}s_{mn}\Delta v_n(\mathbf{x})+\sum_{n=1}^{N}\sum_{l=1}^{N}a_{mnl}\nabla v_n(\mathbf{x})\cdot\nabla v_l(\mathbf{x})+\sum_{n=1}^{N}\mathbf{b}_{mn}\cdot\nabla v_n(\mathbf{x})=0\tag{23}$$

for all $\mathbf{x} \in \Omega$, where

$$s_{mn} = \int_{\underline{k}}^{\overline{k}} \Psi'_n(k)\Psi_m(k)dk, \tag{24}$$

$$a_{mnl} = \int_{\underline{k}}^{\overline{k}} 2k\Psi_n(k)\Psi_m(k)\big(\Psi_l(k) + k\Psi'_l(k)\big)dk, \tag{25}$$

$$\begin{aligned}\mathbf{b}_{mn}(\mathbf{x}) &= \frac{\mathbf{x}-\mathbf{x}_0}{|\mathbf{x}-\mathbf{x}_0|}\int_{\underline{k}}^{\overline{k}} 2\Big[\Big(ik - \frac{1}{|\mathbf{x}-\mathbf{x}_0|}\Big)\Psi'_n(k) + i\Psi_n(k)\Big]\Psi_m(k)dk \\ &= \frac{2i(\mathbf{x}-\mathbf{x}_0)}{|\mathbf{x}-\mathbf{x}_0|}\int_{\underline{k}}^{\overline{k}} k\Psi'_n(k)\Psi_m(k)dk - \frac{2(\mathbf{x}-\mathbf{x}_0)s_{mn}}{|\mathbf{x}-\mathbf{x}_0|^2} + \frac{2i(\mathbf{x}-\mathbf{x}_0)}{|\mathbf{x}-\mathbf{x}_0|}\delta(m,n).\end{aligned} \tag{26}$$

Here, $\delta(m,n)$ is the Kronecker delta

$$\delta(m,n) = \begin{cases} 1 & \text{if } m = n, \\ 0 & \text{if } m \neq n. \end{cases}$$

3.3. Data complementation

The values of $\mathbf{v}(\mathbf{x}) = \begin{bmatrix} v_1(\mathbf{x}), \dots, v_N(\mathbf{x}) \end{bmatrix}^{\mathrm{T}}$ for $\mathbf{x} \in \Gamma$ can be explicitly computed as follows. From Eqs. (13), (15), and (21), we derive

$$g_m(\mathbf{x}) := v_m(\mathbf{x}) = \int_{\underline{k}}^{\overline{k}} \frac{\Psi_m(k)}{k^2} \log\frac{g(\mathbf{x},k)}{u_{\mathrm{inc}}(\mathbf{x},k)}\, dk, \quad m \in \{1,2,\dots,N\}, \tag{27}$$

and

$$h_m(\mathbf{x}) := \partial_z v_m(\mathbf{x}) = \int_{\underline{k}}^{\overline{k}} \frac{\Psi_m(k)}{k^2}\left[\frac{h(\mathbf{x})}{g(\mathbf{x})} - \Big(ik - \frac{1}{|\mathbf{x}-\mathbf{x}_0|}\Big)\frac{z+d}{|\mathbf{x}-\mathbf{x}_0|}\right]dk, \tag{28}$$

for all $\mathbf{x} = (x,y,z) \in \Gamma$ and $m \in \{1,2,\dots,N\}$, where $\mathbf{x}_0 = (0,0,-d)$. While these expressions allow for the direct computation of $\mathbf{v}$ and its normal derivative on Γ, they are not sufficient to determine $\mathbf{v}$ throughout the entire domain Ω because solving second-order equations such as Eq. (23) requires knowledge of the solution on a surface enclosing Ω. However, the data in Eqs. (27) and (28) is well-defined only on Γ, which is located at the bottom Ω. This indicates that the information of $\{v_m\}_{m=1}^N$ on $\partial\Omega \setminus \Gamma$ is crucial but missing. To achieve a stable computation of $\{v_m\}_{m=1}^N$, it is necessary to compensate for this missing data. Since the scattering wave weakens when the receivers are far from the source, we can approximate the scattered wave $u_{\mathrm{sc}}(\mathbf{x},k)$ as zero on $\partial\Omega \setminus \Gamma$. Consequently, $v(\mathbf{x},k)$ vanishes on $\partial\Omega \setminus \Gamma \times [\underline{k}, \overline{k}]$. As a result, for $m = 1,2,\dots,N$, we obtain

$$v_m(\mathbf{x}) = 0 \quad \text{for all } \mathbf{x} \in \partial\Omega \setminus \Gamma. \tag{29}$$

Remark 5. The data supplementation described above is not rigorous but rather an approximation based on the fact that the scattering wave on Γ is stronger than that on $\partial\Omega \setminus \Gamma$. This observation holds because the source location $\mathbf{x}_0 = (0,0,-d)$ is closer to Γ compared to $\partial\Omega \setminus \Gamma$. This supplementation strategy has been successfully applied in our previous works on inverse scattering problems, such as [25–27]. Therefore, we continue to employ this approach.

Combining Eqs. (23), (27), and (29) gives

$$\begin{cases} \displaystyle\sum_{n=1}^N s_{mn}\Delta v_n(\mathbf{x}) + \sum_{n=1}^N\sum_{l=1}^N a_{mnl}\nabla v_n(\mathbf{x})\cdot\nabla v_l(\mathbf{x}) + \sum_{n=1}^N \mathbf{b}_{mn}\cdot\nabla v_n(\mathbf{x}) = 0 & \mathbf{x} \in \Omega, \\ v_m(\mathbf{x}) = g_m(\mathbf{x}) & \mathbf{x} \in \Gamma, \\ \partial_z v_m(\mathbf{x}) = h_m(\mathbf{x}) & \mathbf{x} \in \Gamma, \\ v_m(\mathbf{x}) = 0 & \mathbf{x} \in \partial\Omega \setminus \Gamma. \end{cases} \tag{30}$$

Remark 6. The system composed of all N equations in Eq. (30), for $m \in \{1,\dots,N\}$, provides an approximate model for addressing the inverse scattering problem. This approximation arises from the truncation of high-frequency components in Eq. (20) and the data complementation procedure described in Eq. (29). Although these steps introduce inaccuracy, we view them as a deliberate and necessary regularization strategy. This trade-off substantially mitigates the inherent ill-posedness of the inverse problem, enabling a more stable and feasible numerical solution.

4. The Carleman convexification method

To solve Eq. (30), we employed the Carleman convexification method originally developed in [41] and further advanced in subsequent works [25–27,34].

Recall the matrix $S = (s_{mn})_{m,n=1}^{N}$ as the $N \times N$ matrix whose (m,n)-entry is given by Eq. (24). From [39], it is known that S is invertible. We denote its inverse by $S^{-1} = (\widetilde{s}_{mn})_{m,n=1}^{N}$. Define

$$\widetilde{\mathbf{b}}_{mn} = \sum_{i=1}^{N} \widetilde{s}_{mi}\mathbf{b}_{in}, \quad \widetilde{a}_{mnl} = \sum_{i=1}^{N} \widetilde{s}_{mi}a_{inl}, \quad \text{for } m,n,l \in \{1,\dots,N\}.$$

Using Eq. (23), we obtain the equation

$$\Delta v_m(\mathbf{x}) + \sum_{n=1}^{N} \nabla v_n(\mathbf{x}) \cdot \widetilde{\mathbf{b}}_{mn} + \sum_{n=1}^{N}\sum_{l=1}^{N} \widetilde{a}_{mnl} \nabla v_n(\mathbf{x}) \cdot \nabla v_l(\mathbf{x}) = 0, \tag{31}$$

for $\mathbf{x} \in \Omega$. Eq. (31), combined with Eq. (27), forms an elliptic system:

$$\begin{cases} \Delta v_m(\mathbf{x}) + \sum_{n=1}^{N} \nabla v_n(\mathbf{x}) \cdot \widetilde{\mathbf{b}}_{mn} + \sum_{n=1}^{N}\sum_{l=1}^{N} \widetilde{a}_{mnl} \nabla v_n(\mathbf{x}) \cdot \nabla v_l(\mathbf{x}) = 0, & \mathbf{x} \in \Omega, \\ v_m(\mathbf{x}) = g_m(\mathbf{x}), & \mathbf{x} \in \Gamma, \\ \partial_z v_m(\mathbf{x}) = h_m(\mathbf{x}), & \mathbf{x} \in \Gamma, \\ v_m(\mathbf{x}) = 0 & \mathbf{x} \in \partial\Omega \setminus \Gamma. \end{cases} \tag{32}$$

Remark 7. The system defined in Eq. (32) for $m \in \{1,2,\dots,N\}$ plays a key role to place Problem 2.2 into the framework of the convexification method, and the choice of the basis $\{\Psi_n\}_{n\geq 1}$ is crucial to its formulation. For a given $N \in \mathbb{N}$, recall the matrix $S \in \mathbb{R}^{N\times N}$ whose (m,n)-entry is given by Eq. (24). It was shown in [39] that:

1. The matrix S is invertible;
2. For all $n \geq 1$, the derivative Ψ_n' is not identically zero on the interval $[\underline{k}, \overline{k}]$.

The first property is essential, as the invertibility of S is necessary to define the coefficients in Eq. (32); without knowledge of S^{-1}, the formulation would be incomplete. The second property is equally significant. If $\Psi_n' = 0$ for some n, then important information about Δv_n in the first term of Eq. (30) would be lost. For example, consider replacing the exponential-polynomial basis with more commonly used alternatives such as the Legendre polynomials or the trigonometric basis $\{\phi_n\}_{n\geq 1}$. In these cases, ϕ_1 is a constant function, and thus $\phi_1' \equiv 0$. As a result, the principal term Δv_1 would be absent from Eq. (30), leading to potentially large errors in computing v_1, and consequently affecting the accuracy of the reconstructed function $v(\mathbf{x},k)$ via Eq. (20). This issue is particularly critical because the first term in the truncated series often contributes significantly to the overall reconstruction.

Let $s \geq 4$ be an integer. Note that s is set to be larger than or equal to 4 to ensure that $H^s(\Omega)$ is continuously embedded into $C^2(\overline{\Omega})$. For theoretical purposes, we assume that the target function c is sufficiently smooth so that the true solution to the forward problem u satisfies

$$\|u(\cdot,k)\|_{H^s(\Omega)} < \infty, \quad \text{uniformly for } k \in [\underline{k}, \overline{k}].$$

Additionally, we assume that $|u(x,k)|$ is uniformly bounded below by some positive constant u_0. This condition ensures that the magnitude of the wave field does not fall below this threshold, preventing the measurements from approaching zero or becoming negligibly small. Due to the change of variables in Eq. (15), the function $v(\mathbf{x},k)$ belongs to $H^s(\Omega)$, with its H^s norm uniformly bounded for all $k \in [\underline{k}, \overline{k}]$. Thus, there exists a constant M, depending on the upper bound of $\|u(\cdot,k)\|_{H^s(\Omega)}$ for $k \in [\underline{k}, \overline{k}]$ and the set $\{\Psi_n\}_{n=1}^{N}$, such that

$$\|\mathbf{v}^*\|_{H^s(\Omega)^N} < M,$$

where $\mathbf{v}^*$ is the true solution to Eq. (32). We seek the "best fit" solution to Eq. (32) in the set of admissible solutions

$$B(0,M) = \left\{\boldsymbol{\varphi} \in H^s(\Omega)^N : \|\boldsymbol{\varphi}\|_{H^s(\Omega)^N} < M\right\}, \tag{33}$$

which is the ball centered at the origin with radius M. For positive numbers λ and ϵ, define the Carleman weighted functional $J_{\lambda,\epsilon} : B(0,M) \to \mathbb{R}$

$$\begin{aligned} J_{\lambda,\epsilon}(\boldsymbol{\varphi}) = \sum_{m=1}^{N} \Bigg[& \int_{\Omega} e^{2\lambda(z-r)^2} \left| \Delta\varphi_m(\mathbf{x}) + \sum_{n=1}^{N} \nabla\varphi_n(\mathbf{x}) \cdot \widetilde{\mathbf{b}}_{mn} + \sum_{n=1}^{N}\sum_{l=1}^{N} \widetilde{a}_{mnl} \nabla\varphi_n(\mathbf{x}) \cdot \nabla\varphi_l(\mathbf{x}) \right|^2 d\mathbf{x} \\ & + \lambda^4 e^{2\lambda(R+r)^2} \int_{\Gamma} \left(|\varphi_m - g_m|^2 + |\partial_z\varphi_m - h_m|^2 \right) d\sigma(\mathbf{x}) + \lambda^4 \int_{\partial\Omega\setminus\Gamma} e^{2\lambda(z-r)^2} |\varphi_m|^2 d\sigma(\mathbf{x}) + \epsilon \|\varphi_m\|_{H^s(\Omega)}^2 \Bigg] \end{aligned} \tag{34}$$

for all $\boldsymbol{\varphi} \in B(0,M)$, where $r > R$ is a fixed number and λ is a Carleman parameter.

Remark 8. In the absence of the Carleman weight function $e^{2\lambda(z-r)^2}$, the functional above reduces to the standard least-squares mismatch functional associated with Eq. (32). However, in this unweighted form, this cost functional may possess multiple local minima, making its minimization particularly difficult. Conventional optimization techniques, such as the gradient descent method, are prone to becoming trapped in local minima that are far from the global solution. The core idea of the convexification method is to incorporate the Carleman weight function, which transforms the cost functional into a globally convex form, thereby facilitating the application of standard optimization methods and improving convergence to the true solution.

The theoretical foundation of the convexification method is built upon a rigorous theorem that guarantees $J_{\lambda,\epsilon}$ is strictly convex in the ball $B(0,M)$, and that its global minimizer in this set provides a reliable approximation to the true solution $\mathbf{v}^*$ of Eq. (32). This convexification theorem is fundamentally derived from the following Carleman estimate.

Lemma 1 (Carleman Estimate). *There exist constants $\lambda_0 = \lambda_0(\Omega, r) \geq 1$ and $C = C(\Omega, r) > 0$ such that*

$$\int_\Omega e^{2\lambda(z-r)^2} |\Delta\varphi|^2, d\mathbf{x} \geq C \int_\Omega e^{2\lambda(z-r)^2} (\lambda^3 |\varphi|^2 + \lambda |\nabla\varphi|^2) d\mathbf{x} - C\lambda^3 \int_{\partial\Omega} e^{2\lambda(z-r)^2} |\varphi|^2 d\sigma(\mathbf{x}) - C\lambda \int_\Gamma e^{2\lambda(z-r)^2} |\nabla\varphi|^2 d\sigma(\mathbf{x}). \tag{35}$$

for all functions $\varphi \in C^2(\Omega)$.

The Carleman estimate stated in Lemma 1 is structurally similar to the one presented in [42, Theorem 4.1]. The key distinction lies in the boundary conditions imposed on the function φ. Specifically, [42, Theorem 4.1] assumes that $\varphi|_{\partial\Omega} = 0$ and $\partial_z\varphi|_\Gamma = 0$, whereas Lemma 1 omits the these conditions. To compensate for this relaxation, two negative terms are added to the right-hand side of the Carleman estimate in Eq. (35). Despite this difference, the proof technique used in [42] remains applicable to Lemma 1 with only minor modifications. The main adjustment involves deferring the integration process. Instead of integrating mid-proof, as done in [42, Theorem 4.1], we maintain the Carleman estimate locally at each point in Ω, deriving a pointwise estimate first and performing the integration only at the final stage. This postponed integration strategy aligns with the approach in [28, Theorem 3.1 and Corollary 3.2]. Given the similarity in methodology and the minor nature of the required modifications, we omit the proof of Lemma 1 here. For a more general version of the Carleman estimate, applicable when the Laplacian is replaced by a general elliptic operator, we refer the reader to [43].

We have the theorem.

Theorem 1 (Carleman Convexification Theorem). *Let λ_0 be as given in Lemma 1. The following statements hold:*

1. *For all $\lambda > 1$ and $\epsilon > 0$, the functional $J_{\lambda,\epsilon}$ is Fréchet differentiable, and its derivative $DJ_{\lambda,\epsilon}$ is Lipschitz continuous. That is, there exists a constant L, depending only on Ω, M, and N, such that*

$$\|DJ_{\lambda,\epsilon}(\mathbf{v}_2) - DJ_{\lambda,\epsilon}(\mathbf{v}_1)\|_{H^s(\Omega)^{N\prime}} \leq L\|\mathbf{v}_2 - \mathbf{v}_1\|_{H^s(\Omega)^N}$$

   for all $\mathbf{v}_1, \mathbf{v}_2 \in B(0,M)$.
2. *There exists a constant $\lambda_1 = \lambda_1(M, N, r, \Omega) \geq \lambda_0$ such that for all $\epsilon > 0$ and $\lambda \geq \lambda_1$, the functional $J_{\lambda,\epsilon}$ is strictly convex in $B(0,M)$. Specifically,*

$$\begin{aligned} J_{\lambda,\epsilon}(\mathbf{u}) - J_{\lambda,\epsilon}(\mathbf{v}) - DJ_{\lambda,\epsilon}(\mathbf{v})(\mathbf{u}-\mathbf{v}) \geq (C_1\lambda - C_2) \int_\Omega e^{2\lambda(z-r)^2} \left(|\mathbf{u}-\mathbf{v}|^2 + |\nabla(\mathbf{u}-\mathbf{v})|^2\right) d\mathbf{x} \\ + (C_3\lambda^4 - C_4\lambda^3) \int_\Gamma e^{2\lambda(z-r)^2} (|\mathbf{u}-\mathbf{v}|^2 + |\partial_z(\mathbf{u}-\mathbf{v})|^2)\, d\sigma(\mathbf{x}) + \epsilon\|\mathbf{u}-\mathbf{v}\|^2_{H^s(\Omega)^N}, \end{aligned} \tag{36}$$

   for all $\mathbf{u}, \mathbf{v} \in H$, where C_1, C_2, C_3 and C_4 are positive constants depending only on M, N, r, and Ω. As a result, $J_{\lambda,\epsilon}$ has a unique minimizer in $B(0,M)$, denoted by $\mathbf{v}_{\min}$.
3. *Let $\lambda > \lambda_1$ and define $\Lambda = C_1\lambda - C_2 > 0$. Fix an initial guess $\mathbf{v}^{(0)} \in B(0,M)$ and assume*

$$\left\{\varphi \in B(0,M) : \|\varphi - \mathbf{v}_{\min}\|_{H^s(\Omega)^N} < \|\mathbf{v}^{(0)} - \mathbf{v}_{\min}\|_{H^s(\Omega)^N}\right\} \subset B(0,M).$$

   Define $\eta_0 = \min\{2\Lambda/L^2, 1\}$ and fix a step size $\eta \in (0, \eta_0)$. For each $m \geq 0$, set the iteration

$$\mathbf{v}^{(m+1)} = \mathbf{v}^{(m)} - \eta J'_{\lambda,\epsilon}(\mathbf{v}^{(m)}) \tag{37}$$

   where $J'_{\lambda,\epsilon} : H^s(\Omega)^N \to H^s(\Omega)^N$ is the Rietz representation of $DJ_{\lambda,\epsilon}$. That means,

$$\langle J'_{\lambda,\epsilon}(\mathbf{v}), \varphi\rangle_{H^s(\Omega)^N} = DJ_{\lambda,\epsilon}(\mathbf{v})(\varphi) \quad \text{for all } \mathbf{v}, \varphi \in H^s(\Omega)^N.$$

   Then, there exists a constant $q \in (0,1)$ such that for all $m \geq 0$,

$$\mathbf{v}^{(m)} \in B(0,M) \quad \text{and} \quad \|\mathbf{v}^{(m)} - \mathbf{v}_{\min}\|_{H^s(\Omega)^N} \leq q^{m-1}\|\mathbf{v}^{(0)} - \mathbf{v}_{\min}\|_{H^s(\Omega)^N}.$$

   Consequently, the sequence $\{\mathbf{v}^{(m)}\}_{m\geq 0}$ converges to the unique minimizer $\mathbf{v}_{\min}$ as $m \to \infty$.

The main ideas to establish convexification theorems were originally introduced in [41] and later applied to inverse scattering problems in [26,27]. In those works, some versions of the convexification theorem were formulated for corresponding versions of the cost functional $J_{\lambda,\epsilon}$ that does not include an integral term over the measurement surface Γ and the complementary surfaces $\partial\Omega \setminus \Gamma$. In the absence of these terms, the cost functional is defined on the set

$$\left\{\varphi = \begin{bmatrix}\varphi_1 & \dots & \varphi_N\end{bmatrix}^{\mathrm{T}} \in H^s(\Omega)^N : \|\varphi\|_{H^s(\Omega)^N} < M,\ \varphi_m|_\Gamma = g_m,\ \partial_z\varphi_m|_\Gamma = h_m, \varphi_m|_{\partial\Omega\setminus\Gamma} = 0,\ m = 1, \dots, N\right\}.$$

However, it is nontrivial to verify whether this set is nonempty, whereas the nonemptiness of the set H defined earlier is straightforward. To circumvent this difficulty, we incorporate the integral over Γ and $\partial\Omega \setminus \Gamma$ into the cost functional $J_{\lambda,\epsilon}$.

The proof of Theorem 1 closely follows the methodology presented in [28, Theorem 4.1]. The first part is derived through straightforward algebraic manipulations. The second part builds upon earlier results from [44], and [26, Theorem 5.1], and [28, Theorem

4.1, part 2], with a minor but important modification: in contrast to these prior works, where expressions such as $(C_1\lambda - C_2)$ and $(C_3\lambda^4 - C_4\lambda^3)$ are replaced with a generic constant C, we preserve the explicit dependence on λ to emphasize the crucial role played by the Carleman parameter in the convexity inequality Eq. (32). This modification is justified by adapting the proof technique in [28, Theorem 4.1], with the key difference being the use of the Carleman estimate in Eq. (35) in place of the one used in that reference. The third part of Theorem 1 follows directly from [27, Theorem 2].

We next discuss how close the minimizer of $J_{\lambda,\epsilon}$ is to the true solution of Eq. (32). Let

$$\mathbf{v}^* = \begin{bmatrix} v_1^* & \dots & v_N^* \end{bmatrix}^{\mathrm{T}}$$

denote the exact solution to Eq. (32) corresponding to the noiseless boundary data g_m^* and h_m^*, which are idealized versions of the measured data g_m and h_m, respectively. That is, for each $m \in \{1, \dots, N\}$, the functions v_m^* satisfy the following boundary value problem:

$$\begin{cases} \Delta v_m^*(\mathbf{x}) + \sum_{n=1}^{N} \nabla v_n^*(\mathbf{x}) \cdot \widetilde{\mathbf{b}}_{mn} + \sum_{n=1}^{N}\sum_{l=1}^{N} \widetilde{a}_{mnl} \nabla v_n^*(\mathbf{x}) \cdot \nabla v_l^*(\mathbf{x}) = 0, & \mathbf{x} \in \Omega, \\ v_m^*(\mathbf{x}) = g_m^*(\mathbf{x}), & \mathbf{x} \in \Gamma, \\ \partial_z v_m^*(\mathbf{x}) = h_m^*(\mathbf{x}), & \mathbf{x} \in \Gamma, \\ v_m^*(\mathbf{x}) = 0, & \mathbf{x} \in \partial\Omega \setminus \Gamma. \end{cases} \tag{38}$$

Additionally, we assume the noise level in the measured data is bounded by δ in the following sense

$$\sum_{m=1}^{N} \left(\|g_m - g^*\|_{H^1(\Gamma)} + \|h_m - h_m^*\|_{L^2(\Omega)} \right) < \delta, \tag{39}$$

for some small constant $\delta \ll 1$. Then, using the same arguments of [28, Theorem 4.2], we have

$$\|\mathbf{v}_{\min} - \mathbf{v}^*\|_{H^1(\Omega)^N} \le C\left(\delta + \sqrt{\epsilon}\|\mathbf{v}^*\|_{H^s(\Omega)^N}\right) \tag{40}$$

for some constant C depending only on Ω, M, r, λ, and N. In Eq. (40), we employ the standard Sobolev norm instead of incorporating a Carleman-weighted functional, as was done in our previous work on convexification. This formulation remains valid under the assumption that λ is fixed and the constant C may depend on λ. A direct implication of Eq. (40) is that the global minimizer of $J_{\lambda,\epsilon}$ provides an approximation to the true solution of Eq. (32), with an error bounded by $O(\delta + \sqrt{\epsilon})$.

The WKB method for phase retrieval presented in Section 2, the derivation of the frequency dimensional reduction model in Section 3, the convexification result in Theorem 1, and the error estimate in Eq. (40) collectively motivate the design of Algorithm 1 for solving the phaseless inverse scattering problem.

5. Numerical study

In this section, we highlight key aspects of Algorithm 1's implementation and present several numerical examples to demonstrate its performance.

Algorithm 1 The Carleman convexification method to compute the numerical solution to the phaseless inverse scattering problem.

1: Having the data f in hand, for each k, we minimize the mismatch functional J_k defined in (2.10) using the initial guess $u_{\text{init}}(\mathbf{x}, k) = f(\mathbf{x}, k)e^{ik|\mathbf{x}-\mathbf{x}_0|}$ as in (2.9). The obtained minimizer $u(\mathbf{x}, k)$, $(\mathbf{x}, k) \in \Gamma_L \times [\underline{k}, \overline{k}]$ is the desired wave function including the phase information.

2: Compute $u(\mathbf{x}, k)$ and $\partial_z u(\mathbf{x}, k)$ on Γ, which is the bottom portion of $\partial\Omega$.

3: Choose a cut-off number N, a Carleman parameter λ, and a regularization parameter ϵ. Choose Carleman parameters $\mathbf{x}_0$, β, and λ and a regularization parameter ϵ.

4: Minimize the strictly convex Carleman weighted functional $J_{\lambda,\epsilon}$ defined in (4.4). The minimizer is denoted by $\mathbf{v}_{\text{comp}}(\mathbf{x}) = \begin{bmatrix} v_1^{\text{comp}} & v_2^{\text{comp}} & \dots & v_N^{\text{comp}} \end{bmatrix}^{\mathrm{T}}$, $\mathbf{x} \in \Omega$.

5: By (3.6), we compute $v^{\text{comp}}(\mathbf{x}, k)$ using

$$v^{\text{comp}}(\mathbf{x}, k) = \sum_{n=1}^{N} v_n^{\text{comp}}(\mathbf{x})\Psi_n(k), \tag{41}$$

for $\mathbf{x} \in \Omega$, $k \in [\underline{k}, \overline{k}]$.

6: Due to (3.4), a numerical solution to Problem 2.1 can be computed via

$$c^{\text{comp}}(\mathbf{x}) = 1 - \frac{1}{\overline{k} - \underline{k}} \int_{\underline{k}}^{\overline{k}} \Re e \left[\Delta v^{\text{comp}}(\mathbf{x}, k) + k^2 [\nabla v^{\text{comp}}(\mathbf{x}, k)]^2 + 2\left(ik - \frac{1}{|\mathbf{x} - \mathbf{x}_0|}\right) \nabla v^{\text{comp}}(\mathbf{x}, k) \cdot \frac{\mathbf{x} - \mathbf{x}_0}{|\mathbf{x} - \mathbf{x}_0|} \right] d\mathbf{x} d\theta \tag{42}$$

for all $\mathbf{x} \in \Omega$.

To generate the simulated data, we set $R = 1$, placing the source at $\mathbf{x}_0 = (0, 0, -4)$ and using the wave number interval $[\pi, 2\pi]$. To generate simulated data, the domain $\Omega = (-1, 1)^3$ is discretized using a uniform grid defined as

$$\mathcal{G} = \left\{ (x_i = -1 + (i-1)d_{\mathbf{x}},\ y_j = -1 + (j-1)d_{\mathbf{x}},\ z_t = -1 + (t-1)d_{\mathbf{x}}) : 1 \le i, j, t \le N_{\mathbf{x}} \right\},$$

where $N_{\mathbf{x}} = 21$ and $d_{\mathbf{x}} = 2/(N_{\mathbf{x}} - 1)$. The wave number is interval set to be $[\pi, 2\pi]$ and is uniformly discretized into

$$\mathcal{K} = \{k_1 = \underline{k},\, k_2,\, \ldots,\, k_{N_k} = \overline{k}\},$$

with $k_i = \underline{k} + (i-1)\frac{\overline{k}-\underline{k}}{N_k - 1}$ and $N_k = 121$. The forward problem is addressed by reformulating the Helmholtz model Eq. (3) into the Lippmann-Schwinger integral equation, following the approach in [33]. This integral equation is then numerically solved using the volume integral equation method developed in [45,46]. Let $u^*(\mathbf{x}, k)$, with $\mathbf{x} \in \mathcal{G}$ and $k \in \mathcal{K}$, denote the exact solution. We define the noisy data as

$$f(\mathbf{x}, k) = |u^*(\mathbf{x}, k)|(1 + \delta\, \mathrm{rand}),$$

for $(\mathbf{x}, k) \in (\Gamma_L \cap \mathcal{G}) \times \mathcal{K}$, where $\delta = 10\%$ and rand represents a uniformly distributed random variable in the interval $[-1, 1]$. In this section, we set $L = 0.28$. For the artificial parameters involved in solving the inverse problem, we select $N = 7$, $\lambda = 1.1$, and $\epsilon = 10^{-5.75}$. These values are determined through a trial-and-error process. They are consistent with the corresponding set of parameters in [27]. Specifically, we use Test 1 as a reference case to manually identify a suitable set of parameters, which are then consistently applied across all subsequent tests.

5.1. Numerical implementation of phase retrieval

In Step 1 of Algorithm 1, we solve the optimization problem by discretizing the cost functional J_k, defined in Eq. (11) using a grid-based approach, where the integrals are approximated in a manner similar to the Riemann sum in multivariable calculus. For simplicity, we use MATLAB's built-in optimization function `fminunc`, which implements the quasi-Newton method, to minimize the cost functional. The optimization process is set up using the following code:

```
options = optimoptions(@fminunc, 'Algorithm', 'quasi-newton', 'UseParallel', true);
J = @(U) Cost_Phase_Retrieval(U, phaseless_data, k, normf);
U = fminunc(J, U, options);
```

Here, `Cost_Phase_Retrieval` is the function that evaluates the cost functional given the current estimate U, the phaseless data, and other problem parameters. The optimization method iteratively updates the wave field estimate U, utilizing parallel computation to accelerate the process. The objective is to find the optimal wave field that minimizes the discrepancy between the model and the data while satisfying the governing equation. The optimization process terminates when the change in the optimization variables is from the last iteration to the current one is smaller than 10^{-6}.

As a representative example, we demonstrate the recovery of the lost phase. Starting from the noisy data f in Test 1, the optimization is initialized with $u_{\text{init}} = f(\mathbf{x}, k)e^{ik|\mathbf{x}-\mathbf{x}_0|}$, and `fminunc` is applied to minimize the cost. The resulting reconstruction of the complex-valued wave function u, including both its real and imaginary parts, is presented in Fig. 2.

The numerical results in Fig. 2 demonstrate the effectiveness of the phase retrieval strategy. Despite the presence of 10% noise in the measured data (Fig. 2(a)), the reconstructed wave field (Fig. 2(c) and (e)) closely approximates the true solution (Fig. 2(b) and (d)) in both the real and imaginary components. The method successfully preserves key structural features, such as spatial distribution and amplitude. In particular, the imaginary part of the reconstruction captures the peak profile with good accuracy, while the real part accurately recovers the expected dip pattern. The plot in Fig. 2(f) shows the difference between the true and reconstructed wave function, specifically $|u^* - u|$, highlighting the error in the phase recovery process. This plot provides a clear visualization of the reconstruction accuracy, demonstrating how closely the reconstructed wave function matches the true function, even in the presence of noisy data.

Although the input data in Fig. 2(a) appears heavily degraded, the reconstructed real and imaginary parts (Fig. 2(c) and (e)) exhibit a clear improvement in quality. This enhancement is primarily attributed to the structure of the cost functional J_k, which incorporates a regularization term involving the Laplacian of the wave field (see the first term on the right-hand side of Eq. (11)). This term promotes smoothness by penalizing irregular or non-differentiable behavior, resulting in reconstructions that are inherently smoother than the raw, noisy magnitude data. Despite this regularization, some residual noise persists in the reconstructed fields. This is due to the high noise level (10%) in the input and the effect of the data fidelity term in Eq. (11), which constrains the solution to remain close to the measured data f, thereby preserving some of its noise features. To address this, a Fourier filtering procedure (see Eq. (20)) is employed in a subsequent step to suppress remaining high-frequency components, further improving the stability and accuracy of the final reconstruction.

5.2. Numerical implementation of the convexification method

The Carleman convexification framework is implemented in Step 4 of Algorithm 1. The goal of this step is to compute the vector $\mathbf{v}_{\text{comp}}$, whose components represent the Fourier coefficients of the function v defined in Eq. (15). This vector corresponds to the solution of problem Eq. (30), which is equivalent to Eq. (32). However, it is important to note that Eq. (32) involves the inverse matrix S^{-1}, and numerical observations indicate that some of its entries can attain large magnitudes, potentially degrading the accuracy of the final reconstruction. To mitigate this issue and avoid unnecessary numerical errors, we opt to solve Eq. (30) directly rather than Eq. (32).

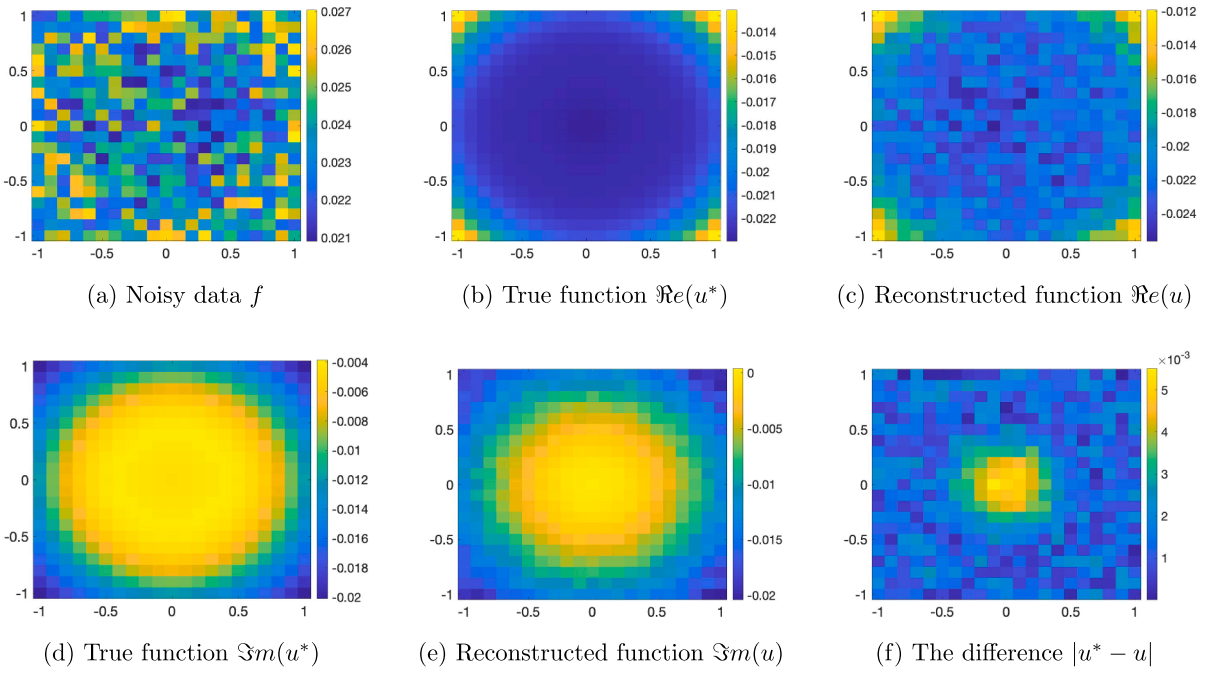

(a) Noisy data f (b) True function $\Re e(u^*)$ (c) Reconstructed function $\Re e(u)$

(d) True function $\Im m(u^*)$ (e) Reconstructed function $\Im m(u)$ (f) The difference $|u^* - u|$

Fig. 2. Reconstruction of the wave function $u(\mathbf{x}, k)$ on Γ with $k = \underline{k}$, showing both real and imaginary parts from magnitude-only data. The data in (a) corresponds to Test 1 with a noise level of 10%.

In this case, we reformulate the cost functional $J_{\lambda,\epsilon}$ as follows:

$$J_{\lambda,\epsilon}(\varphi) = \sum_{m=1}^{N} \left[\int_{\Omega} e^{2\lambda(z-r)^2} \Big| \sum_{n=1}^{N} s_{mn} \Delta\varphi_n(\mathbf{x}) + \sum_{n=1}^{N}\sum_{l=1}^{N} a_{mnl} \nabla\varphi_n(\mathbf{x}) \cdot \nabla\varphi_l(\mathbf{x}) + \sum_{n=1}^{N} \mathbf{b}_{mn} \cdot \nabla\varphi_n(\mathbf{x}) \Big|^2 d\mathbf{x} + \lambda^4 e^{2\lambda(R+r)^2} \int_{\Gamma} \left(|\varphi_m - g_m|^2 + |\partial_z \varphi_m - h_m|^2 \right) d\sigma(\mathbf{x}) + \lambda^4 \int_{\partial\Omega\setminus\Gamma} e^{2\lambda(z-r)^2} |\varphi_m|^2 d\sigma(\mathbf{x}) + \epsilon \|\varphi_m\|^2_{H^2(\Omega)} \right] \tag{43}$$

for all $\varphi \in H$. Without confusion, we continue to denote this functional by $J_{\lambda,\epsilon}$. We also note that, unlike in the theoretical part, which requests $s \geq 4$, we use the regularization norm $H^2(\Omega)$. This significantly simplifies the implementation without reducing the quality of the final reconstruction.

Minimizing the functional $J_{\lambda,\epsilon}$ in Eq. (43) requires an initial guess $\mathbf{v}^{(0)}$. According to the convexification theorem, this initial guess does not need to be close to the global minimizer of $J_{\lambda,\epsilon}$; the only requirement is that $\mathbf{v}^{(0)} \in H$. Following the approach in [27], we simplify the construction of $\mathbf{v}^{(0)}$ by omitting the nonlinear term $\sum_{n=1}^{N}\sum_{l=1}^{N} a_{mnl} \nabla\varphi_n(\mathbf{x}) \cdot \nabla\varphi_l(\mathbf{x})$ from Eq. (43). That means, we define $\mathbf{v}^{(0)}$ as the minimizer of the simplified strictly convex cost functional:

$$J^{(0)}_{\lambda,\epsilon}(\varphi) = \sum_{m=1}^{N} \left[\int_{\Omega} e^{2\lambda(z-r)^2} \Big| \sum_{n=1}^{N} s_{mn} \Delta\varphi_n(\mathbf{x}) + \sum_{n=1}^{N} \mathbf{b}_{mn} \cdot \nabla\varphi_n(\mathbf{x}) \Big|^2 d\mathbf{x} + \lambda^4 \int_{\partial\Omega\setminus\Gamma} e^{2\lambda(z-r)^2} |\varphi_m|^2 d\sigma(\mathbf{x}) + \lambda^4 e^{2\lambda(R+r)^2} \int_{\Gamma} \left(|\varphi_m - g_m|^2 + |\partial_z \varphi_m - h_m|^2 \right) d\sigma(\mathbf{x}) + \epsilon \|\varphi_m\|^2_{H^2(\Omega)} \right] \tag{44}$$

for all $\varphi \in B(0, M)$. Having the initialized vector $\mathbf{v}^{(0)}$ in hand, we compute the minimizer by the gradient descent method using the formula Eq. (37). This requires us to compute the derivative of $J_{\lambda,\epsilon}$. In the implementation, we compute the derivative in finite difference by regarding $J_{\lambda,\epsilon}$ as a function of $N_{\mathbf{x}}^3 N$ variables. The discretized version of $\varphi \in H^2(\Omega)^N$ is

$$\varphi := \left\{ \varphi_m(x_i, y_j, z_t) : 1 \leq i, j, t \leq N_x, 1 \leq m \leq N \right\}$$

and that of $J_{\lambda,\epsilon}$ is

$$
\begin{aligned}
J_{\lambda,\epsilon}(\varphi) = \sum_{m=1}^{N} \Bigg[& d_{\mathbf{x}}^3 \sum_{i,j,t=2}^{N_{\mathbf{x}}-1} e^{2\lambda(z_t-r)^2} \Big| \sum_{n=1}^{N} s_{mn} \Delta^{d_{\mathbf{x}}} \varphi_n(x_i,y_j,z_t) + \sum_{n=1}^{N}\sum_{l=1}^{N} a_{mnl} \nabla^{d_{\mathbf{x}}} \varphi_n(x_i,y_j,z_t) \cdot \nabla^{d_{\mathbf{x}}} \varphi_l(x_i,y_j,z_t) + \sum_{n=1}^{N} \mathbf{b}_{mn} \cdot \nabla^{d_{\mathbf{x}}} \varphi_n(x_i,y_j,z_t) \Big|^2 \\
& + \lambda^4 e^{2\lambda(R+r)^2} d_{\mathbf{x}}^2 \sum_{i,j=1}^{N_{\mathbf{x}}} \left(|\varphi_m(x_i,y_j,z_1) - g_m(x_i,y_j,z_1)|^2 + |\partial_z^{d_{\mathbf{x}}} \varphi_m(x_i,y_j,z_1) - h_m(x_i,y_j,z_1)|^2 \right) \\
& + \lambda^4 d_{\mathbf{x}}^2 \sum_{i,j=1}^{N_{\mathbf{x}}} e^{2\lambda(z_{N_{\mathbf{x}}}-r)^2} |\varphi_m(x_i,y_j,z_{N_{\mathbf{x}}})|^2 d\sigma(\mathbf{x}) + \lambda^4 d_{\mathbf{x}}^2 \sum_{i,j\in\{1,N_{\mathbf{x}}\}} \sum_{t=1}^{N_{\mathbf{x}}} e^{2\lambda(z_t-r)^2} |\varphi_m(x_i,y_j,z_t)|^2 d\sigma(\mathbf{x}) \\
& + \epsilon d_{\mathbf{x}}^3 \sum_{i,j,t=2}^{N_{\mathbf{x}}-1} |\varphi_m(x_i,y_j,z_t)|^2 + |\nabla^{d_{\mathbf{x}}} \varphi_m(x_i,y_j,z_t)|^2 + |\Delta^{d_{\mathbf{x}}} \varphi_m(x_i,y_j,z_t)|^2 \Bigg].
\end{aligned}
\tag{45}
$$

In Eq. (45),

$$
\nabla^{d_{\mathbf{x}}} \varphi(x_i,y_j,z_t) = \begin{bmatrix} \partial_x^{d_{\mathbf{x}}} \varphi(x_i,y_j,z_t) \\ \partial_y^{d_{\mathbf{x}}} \varphi(x_i,y_j,z_t) \\ \partial_z^{d_{\mathbf{x}}} \varphi(x_i,y_j,z_t) \end{bmatrix} = \begin{bmatrix} \frac{\varphi(x_{i+1},y_j,z_t) - \varphi(x_{i-1},y_j,z_t)}{2d_{\mathbf{x}}} \\ \frac{\varphi(x_i,y_{j+1},z_t) - \varphi(x_i,y_{j-1},z_t)}{2d_{\mathbf{x}}} \\ \frac{\varphi(x_i,y_j,z_{t+1}) - \varphi(x_i,y_j,z_{t-1})}{2d_{\mathbf{x}}} \end{bmatrix},
$$

$$
\begin{aligned}
\Delta^{d_{\mathbf{x}}} \varphi(x_i,y_j,z_t) = \frac{1}{d_{\mathbf{x}}^2} \Big[& \varphi(x_{i+1},y_j,z_t) + \varphi(x_{i-1},y_j,z_t) + \varphi(x_i,y_{j+1},z_t) \\
& + \varphi(x_i,y_{j-1},z_t) + \varphi(x_i,y_j,z_{t+1}) + \varphi(x_i,y_j,z_{t-1}) - 6\varphi(x_i,y_j,z_t) \Big].
\end{aligned}
$$

We can interpret the discretized form in Eq. (45) as a polynomial in the variables

$$
\left\{ \varphi_m(x_i,y_j,z_t) \,:\, 1 \le i,j,t \le N_{\mathbf{x}},\ 1 \le m \le N \right\},
$$

allowing us to compute its derivative explicitly.

5.3. Numerical examples

We present three numerical solutions to the phaseless inverse scattering problem due to Algorithm 1.

5.3.1. Test 1

We define the true profile of the dielectric constant as

$$
c^{\text{true}}(x,y,z) = \begin{cases} 5 & \text{if } x^2+y^2 < 0.25^2 \text{ and } |z+0.65| < 0.05, \\ 1 & \text{otherwise.} \end{cases}
$$

The true and reconstructed dielectric profiles are visualized in Fig. 3.

Fig. 3 illustrates the effectiveness of the proposed reconstruction method in recovering the dielectric constant $c(\mathbf{x})$ from phaseless measurements corrupted with 10% noise. The 3D visualizations in Fig. 3(a) and (b) show that the reconstructed scatterer closely matches the true inclusion in both position and geometry. Additionally, the cross-sectional views in Fig. 3(c) and (d) demonstrate that the reconstruction accurately preserves the spatial distribution and peak amplitude of the dielectric profile. The reconstructed function c achieves a maximum value of 5.0689, corresponding to a relative error of 1.38%. These results highlight the robustness and accuracy of the method, confirming its potential to produce high-quality reconstructions even from limited and noisy phaseless data.

5.3.2. Test 2

We next test the case of two inclusions. The true dielectric constant function is given by

$$
c^{\text{true}} = \begin{cases} 5 & (x-0.5)^2+y^2 < 0.25^2 \text{and} |z+0.65| < 0.05, \\ 4.5 & (x+0.5)^2+y^2 < 0.25^2 \text{and} |z+0.65| < 0.05, \\ 1 & \text{otherwise.} \end{cases}
$$

The true and reconstructed dielectric profiles are visualized in Fig. 4.

Fig. 4 highlights the effectiveness of the proposed method in reconstructing multiple inclusions from phaseless data corrupted by 10% noise. The 3D isosurface visualizations in Fig. 4(a) and (b) demonstrate that the reconstructed scatterers closely replicate the true geometry and spatial distribution of the targets. Importantly, the method accurately preserves the separation and relative sizes of the two inclusions. The cross-sectional views in Fig. 4(c) and (d) further validate the reconstruction quality, revealing that both the amplitude and localization of the high-contrast regions are well recovered. Quantitatively, the maximum value of the first inclusion centered at $(0.5, 0, -0.65)$ is 6.1436, yielding a relative error of 22.87%, while the second inclusion centered at $(-0.5, 0, -0.65)$ attains a maximum of 5.1815, with a relative error of 15.14%. These reconstruction errors are considered acceptable, especially given the high noise level and the severe ill-posedness of the inverse problem with single-sided measurements.

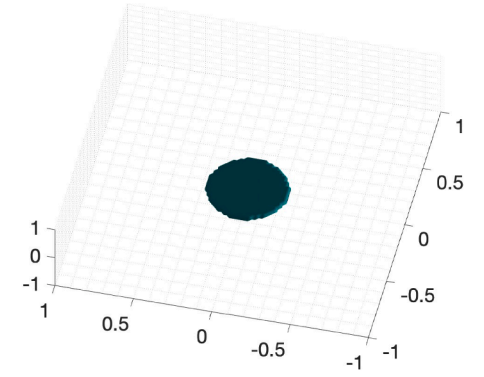

(a) 3D view of the true scatterer

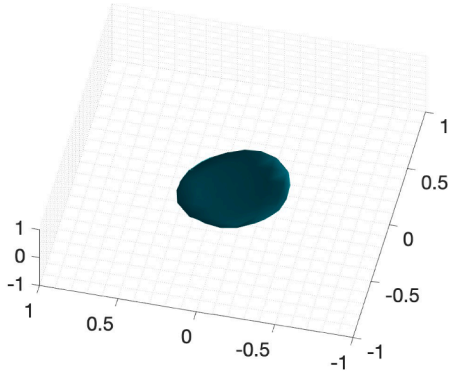

(b) 3D view of the reconstructed scatterer

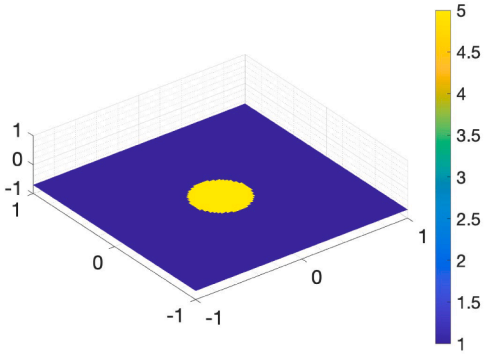

(c) Cross-sectional view of the function c^{true}

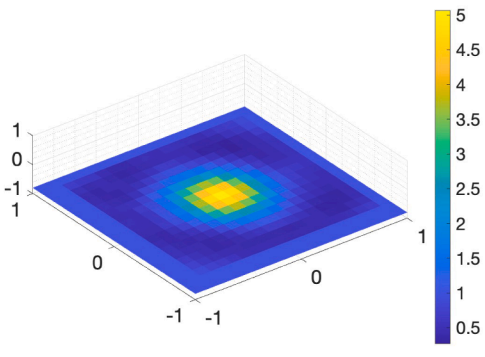

(d) Cross-sectional view of the function c^{comp}

Fig. 3. Test 1. Visualization of the true and reconstructed dielectric constant $c(\mathbf{x})$, $\mathbf{x} \in \Omega$. Subfigures (a) and (b) show 3D views of the true and reconstructed scatterers, respectively. Subfigures (c) and (d) display cross-sectional slices of the corresponding dielectric profiles. The reconstruction demonstrates strong agreement with the true target in both shape and amplitude. The dielectric function $c(\mathbf{x})$ was reconstructed from phaseless data containing 10% noise.

5.3.3. Test 3

Next, we consider the case of two rectangular inclusions. The true dielectric constant function is given by

$$c^{\text{true}} = \begin{cases} 3.2 & \max\{0.25|x|, |y+0.5|\} < 0.2 \text{and} |z+0.65| < 0.05, \\ 3.2 & \max\{0.25|x|, |y-0.5|\} < 0.2 \text{and} |z+0.65| < 0.05, \\ 1 & \text{otherwise.} \end{cases}$$

The true and reconstructed dielectric profiles are visualized in Fig. 5.

Fig. 5 demonstrates the capability of the proposed method to accurately reconstruct elongated inclusions from noisy phaseless data. The 3D views in Fig. 5(a) and (b) reveal that the reconstructed scatterers closely resemble the true targets in both shape and orientation, effectively capturing their elongated geometry and spatial arrangement. The cross-sectional slices in Fig. 5(c) and (d) confirm that the reconstructed dielectric profile approximates the correct locations and amplitudes of the inclusions. The maximum value of the computed function c is 3.5151, corresponding to the relative error 9.85%. Although some smoothing is visible due to the regularization and the presence of 10% noise, the method successfully preserves the key features of the underlying structure. These results further validate the robustness of the algorithm, particularly in recovering complex shapes under limited and noisy measurement conditions.

These numerical experiments confirm that the proposed method can successfully recover the dielectric constant from phaseless data, even in the presence of noise and multiple inclusions. The reconstructions demonstrate both geometric accuracy and stability, thereby validating the overall effectiveness of our algorithm on a uniform mesh with moderate noise levels.

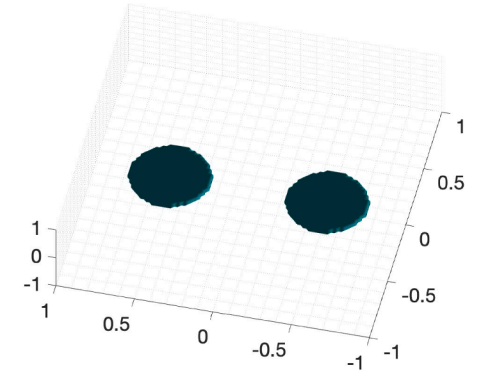

(a) 3D view of the true scatterer

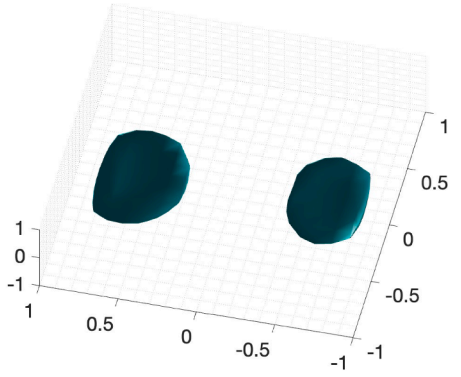

(b) 3D view of the reconstructed scatterer

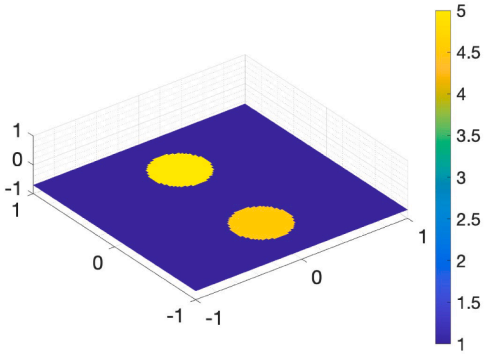

(c) Cross-sectional view of the function c^{true}

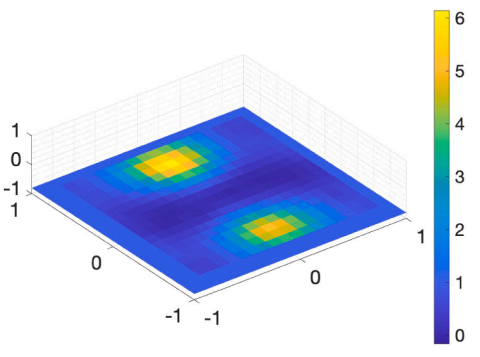

(d) Cross-sectional view of the function c^{comp}

Fig. 4. Test 2. The true and reconstructed dielectric constant $c(\mathbf{x})$, $\mathbf{x} \in \Omega$. Subfigures (a) and (b) display 3D views of the true and reconstructed scatterers, while (c) and (d) present cross-sectional views of their respective dielectric profiles. The reconstructed result successfully captures both the spatial location and amplitude of the true inclusions, demonstrating strong robustness to noise. The reconstruction was performed using phaseless data corrupted with 10% noise.

6. Additional algorithmic analysis

While the above results provide a solid baseline demonstration, further analysis is needed to understand how various parameters affect the performance of the algorithm. In this section, we investigate the influence of the Fourier cut-off number N, compare our method with conventional least-squares optimization, study the sensitivity of the reconstruction to different noise levels, and examine the applicability of the technique on nonuniform meshes. These additional studies provide deeper insight into the robustness and flexibility of the proposed approach.

6.1. Effect of Fourier cut-off number N

The Fourier cut-off number N plays a crucial role in the computational cost of our algorithm since it is the number of equations in Eq. (32). Hence, it is interesting to investigate the impact of N on the accuracy of the reconstruction process. Specifically, N determines the number of Fourier modes used to represent the function v. By varying N, we aim to explore how including more or fewer Fourier modes affects the quality and stability of the reconstructed data. We conduct a series of tests with different values of N to examine their effect on reconstruction accuracy, using the data from Test 1 as a case study. Smaller values of N may limit the precision of the reconstruction, while larger values allow for a more detailed and accurate representation of the underlying model. The results of these tests are presented in Fig. 6, where we compare the reconstruction accuracy for $N = 5$, $N = 8$, and $N = 9$.

As observed from the reconstruction results, smaller values of the cut-off parameter (e.g., $N = 5$ in Fig. 6(a)) generally yield lower reconstruction accuracy compared to larger values (e.g., $N = 8$ and $N = 9$ in Fig. 6(b) and (c)). These results suggest that the reconstruction becomes stable and reliable when $N \geq 7$, whereas smaller values may not capture sufficient Fourier modes to produce high-quality reconstructions.

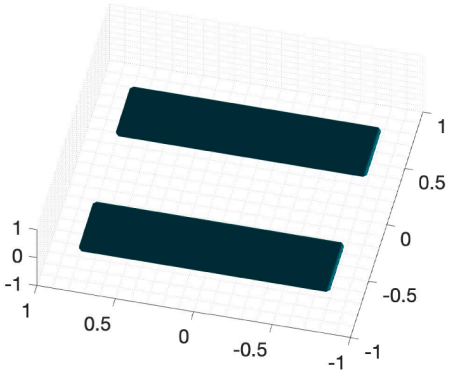

(a) 3D view of the true scatterer

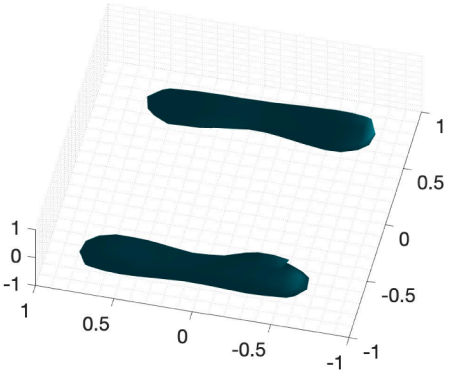

(b) 3D view of the reconstructed scatterer

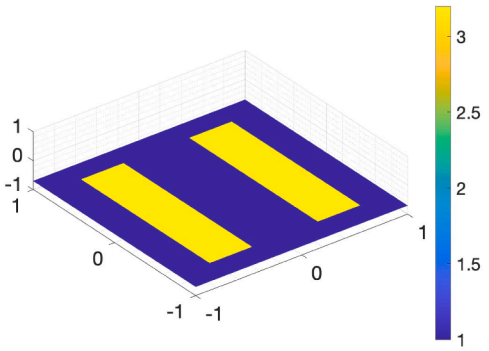

(c) Cross-sectional view of the function c^{true}

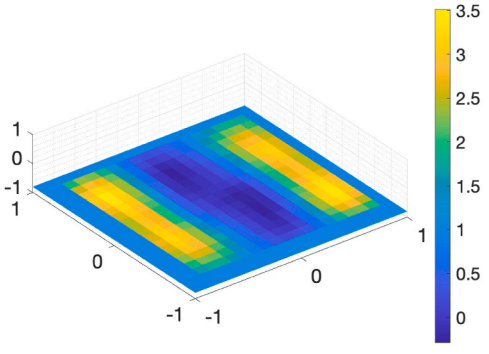

(d) Cross-sectional view of the function c^{comp}

Fig. 5. Test 3. The true and reconstructed dielectric constant $c(\mathbf{x})$, $\mathbf{x} \in \Omega$. Subfigures (a) and (b) show 3D isosurfaces of the true and reconstructed scatterers, respectively, while (c) and (d) display cross-sectional slices of their corresponding dielectric profiles. The reconstruction accurately recovers the elongated shape, spatial separation, and amplitude of both inclusions. These results highlight the method's robustness and effectiveness in handling phaseless data with 10% noise.

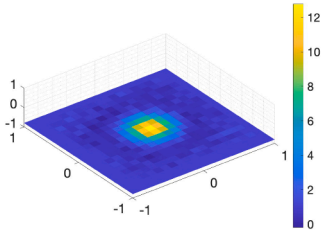

(a) $N = 5$

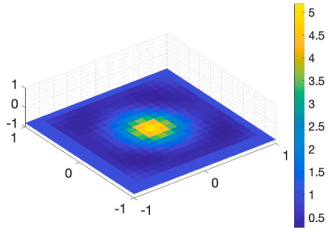

(b) $N = 8$

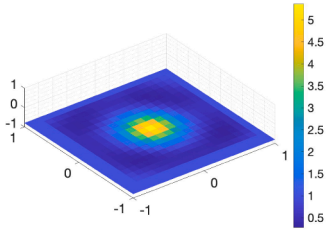

(c) $N = 9$

Fig. 6. Cross-section views of c^{comp} of Test 1 for different Fourier cut-off values N.

6.2. Comparison with conventional least-squares optimization

It is also instructive to compare our proposed method with more traditional approaches. We perform a comparison against a conventional least-squares optimization method. In particular, we consider the numerical solution c^{opt} as the minimizer of the following cost functional:

$$J(f) = \arg\min_{c} \int_{\underline{k}}^{\overline{k}} \int_{\Gamma_L} \left| |u_c(\mathbf{x}, k)|^2 - |f(\mathbf{x}, k)|^2 \right|^2 d\mathbf{x}\, dk + \epsilon \|c\|^2_{H^2(\Omega)}, \tag{46}$$

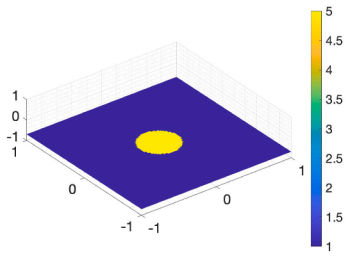

(a) Cross-sectional view of the function c^{true}

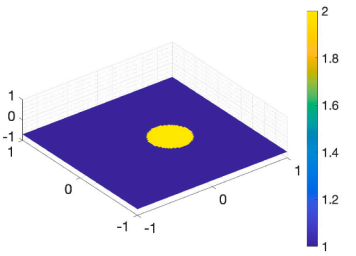

(b) Cross-section of c^{init}

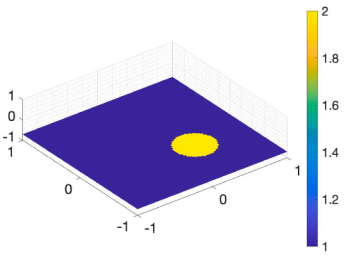

(c) Cross-section of c^{init}

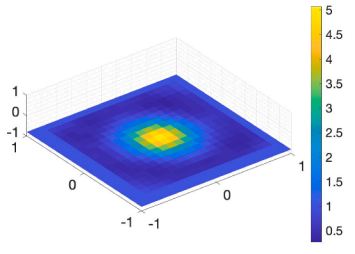

(d) Cross-sectional view of the function c^{comp} by the proposed method

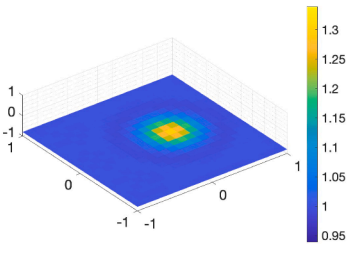

(e) Cross-section of c^{opt}

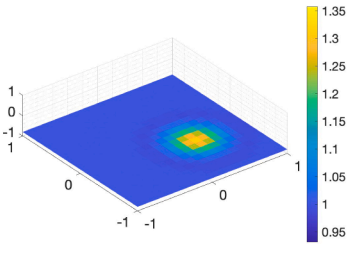

(f) Cross-section of c^{opt}

Fig. 7. Reconstruction of the coefficient $c(\mathbf{x})$ using the conventional least-squares method and the proposed WKB–Carleman method. (a) and (d): cross-sectional views of the true coefficient c^{true} and the corresponding reconstruction c^{comp} obtained by the proposed method, respectively. (b) and (c): two different cross-sections of the initial guess c^{init}. (e) and (f): corresponding reconstructions c^{opt} obtained by minimizing the cost functional J defined in Eq. (46).

where u_c is the solution of the forward problem Eq. (3), and $\epsilon = 10^{-3}$ is a regularization parameter. The H^2-norm regularization is employed to mitigate the sensitivity of the solution to measurement noise. In contrast to the proposed method, the conventional least-squares approach requires a reasonably accurate initial guess c^{init} for the true coefficient. To illustrate this, we present a numerical example where the true coefficient c^{true} corresponds to a single spherical inclusion, as in Test 1. The results demonstrate that the quality of the reconstruction is susceptible to the chosen initial guess and may fail to yield reliable solutions without strong a priori information. Note that using different values of the regularization parameter, namely $\epsilon = 10^{-6}$, provides similar results.

In Fig. 7, we present the reconstruction of the coefficient function $c(\mathbf{x})$ using the conventional least-squares approach. The initial guesses c^{init} in Fig. 7(c) and (d) are deliberately chosen to contain a spherical inclusion with radius $r = 0.25$, centered at $(0, 0.2, -0.65)$ and $(0, -0.3, 0.3)$ respectively. The value of c^{init} is 2 inside the inclusion. The true coefficient corresponds to an inclusion centered at $(0, 0)$ in the (x, y) plane, with contrast value 5. The corresponding reconstructions c^{opt} in Fig. 7(e) and (f) demonstrate a notable deviation from the true coefficient profile, both in terms of spatial location and contrast. In particular, the reconstructions fail to capture the correct position of the inclusion and significantly underestimate its contrast. This illustrates a key drawback of the least-squares method in the phaseless inverse setting: the solution is highly sensitive to the initial guess and may converge to a local minimum far from the true coefficient, even when some structural information is known *a priori*.

6.3. Sensitivity to measurement noise and stability

From the convexification analysis, the global minimizer $\mathbf{v}_{\min}$ of the Carleman-weighted functional $J_{\lambda,\epsilon}$ remains close to the true vector-valued solution $\mathbf{v}^*$ when the noise level $\delta \ll 1$ and the regularization parameter $\epsilon > 0$; see Eq. (40). This estimate implies that the recovered Fourier-coefficient vector $\mathbf{v}_{\min}$ is stable with respect to the data noise for fixed ϵ. Since the coefficient c is reconstructed from $\mathbf{v}$ using the identity derived from Eq. (43) (see Step 6 of Algorithm 1), the stability of $\mathbf{v}_{\min}$ directly transfers to the stability of c^{comp} after the application of spatial derivatives and averaging over $k \in [\underline{k}, \bar{k}]$. We now numerically confirm this theoretical result by recomputing the reconstruction in Test 2 under noise levels 2% and 3%, with the outcomes displayed in Fig. 8.

Fig. 8 illustrates the convergence behavior of the proposed method as the noise level decreases. With 10% noise, the reconstruction still captures the correct location and general shape of the inclusions, though the contrast is somewhat blurred. When the noise level is reduced to 3% and 2%, the reconstructed profiles become increasingly sharp and their amplitudes approach those of the true coefficient. This trend is fully consistent with the stability estimate Eq. (40), which guarantees that the error in the recovered

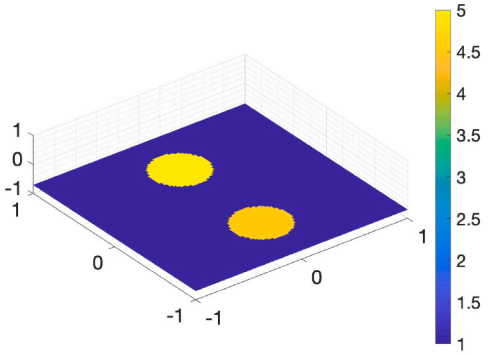

(a) Cross-sectional view of the function c^{true} in test 2, see Figure 4c.

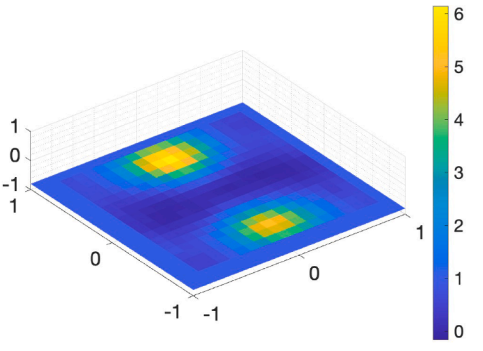

(b) Cross-sectional view of the function c^{comp} using data with 10% noise, see Figure 4d.

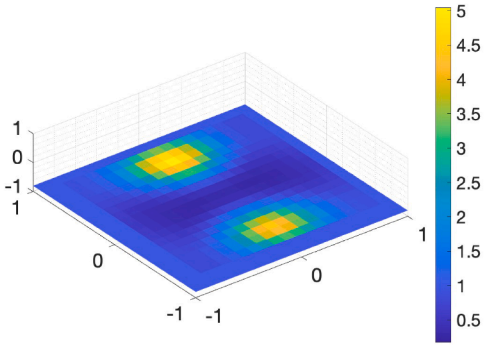

(c) Cross-sectional view of the function c^{comp} using data with 2% noise.

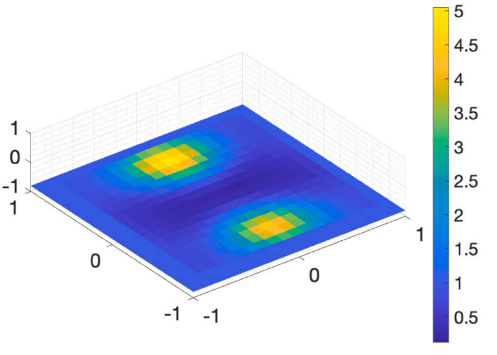

(d) Cross-sectional view of the function c^{comp} using data with 3% noise, see Figure 4d.

Fig. 8. Cross-sectional reconstructions of the dielectric constant under different noise levels. Subfigure (a) shows the true profile from Test 2 for reference. Subfigures (b)–(d) display the computed reconstructions c^{comp} using noisy data with 10%, 2%, and 3% noise, respectively. As the noise level decreases, the reconstructed inclusions converge toward the true profile, both in shape and amplitude, illustrating the stability and convergence of the proposed method with respect to noisy data.

vector $\mathbf{v}_{\min}$ is proportional to the noise level δ (up to the regularization term). Consequently, the reconstruction c^{comp} converges to an approximation of the ground truth as $\delta \to 0$, confirming both the theoretical prediction and the robustness of the algorithm in practice.

6.4. Non-uniform mesh

All of the results above were obtained using a finite-difference scheme on the uniform mesh introduced at the beginning of Section 5. We next examine the performance of the method on non-uniform meshes, which are often more relevant for practical computations. To test the method on a non-uniform mesh, we refined the grid near the origin in the (x, y)-plane and near the measurement surface in the z-direction. Specifically, we set $N_x = N_y = 21$ and $N_z = 21$ with domain $\Omega = (-R, R)^3$, where $R = 1$. The non-uniform coordinates were generated as follows. For the horizontal directions, we introduced the graded mapping

$$s_i = -1 + \frac{2(i-1)}{N_x - 1}, \qquad x_i = R\,\text{sign}(s_i)\,|s_i|^{\gamma_c}, \quad y_j = R\,\text{sign}(s_j)\,|s_j|^{\gamma_c},$$

with grading parameter $\gamma_c = 1.03$, which produces slightly denser spacing near the center of the domain. For the vertical direction, we set

$$t_k = \frac{k-1}{N_z - 1}, \qquad z_k = -R + 2R\,t_k^{\gamma_z},$$

with $\gamma_z = 1.05$, yielding a mesh refined toward the bottom measurement surface.

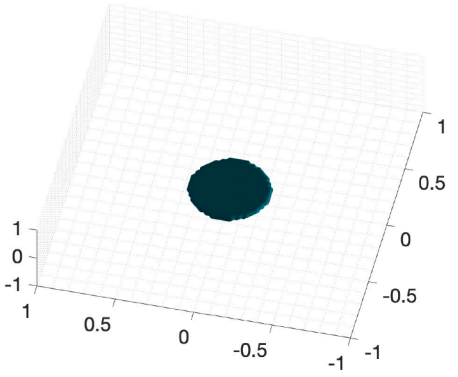

(a) 3D view of the true scatterer

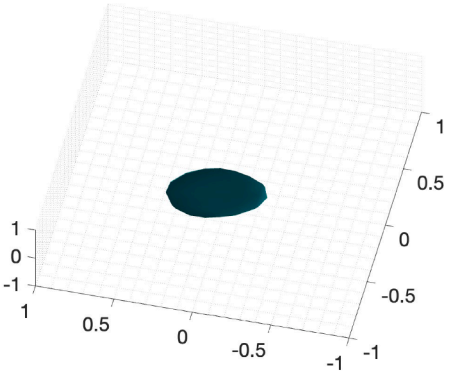

(b) 3D view of the reconstructed scatterer with non-uniform mesh

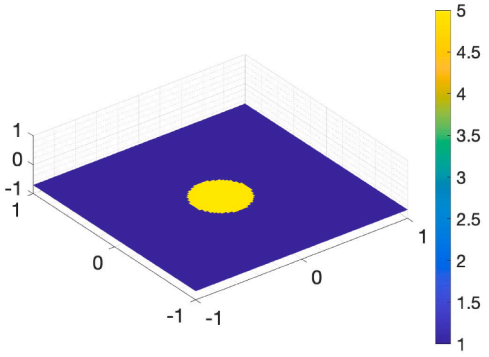

(c) Cross-sectional view of the function c^{true}

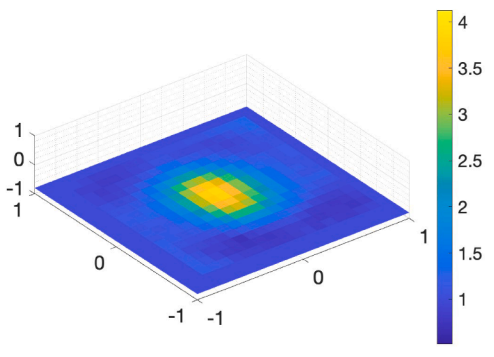

(d) Cross-sectional view of the function c^{comp} with non-uniform mesh

Fig. 9. Test 1. Subfigures (a) and (b) show 3D views of the true scatterer and the reconstructed scatterer obtained using a non-uniform mesh. Subfigures (c) and (d) display cross-sectional slices of the dielectric profiles c^{true} and c^{comp}, respectively. The data contains 10% noise. The reconstruction on the non-uniform mesh captures the location and overall shape of the inclusion, but the result is less accurate in amplitude compared to the uniform mesh case. Nevertheless, the reconstruction remains acceptable and demonstrates that the proposed method can be applied on non-uniform grids.

On a non-uniform grid, the spacing between points varies, so the derivative formulas must be adapted. For the first derivative in the x-direction at an interior point x_i, we use the second-order three-point formula

$$\partial_x f(x_i, y_j, z_k) \approx \frac{h_i^x}{h_{i-1}^x(h_{i-1}^x + h_i^x)} f_{i-1,j,k} - \frac{h_i^x - h_{i-1}^x}{h_{i-1}^x h_i^x} f_{i,j,k} + \frac{h_{i-1}^x}{h_i^x(h_{i-1}^x + h_i^x)} f_{i+1,j,k},$$

where $h_{i-1}^x = x_i - x_{i-1}$ and $h_i^x = x_{i+1} - x_i$. For the second derivative, the corresponding three-point formula is

$$\partial_{xx} f(x_i, y_j, z_k) \approx \frac{2}{h_{i-1}^x + h_i^x}\left(\frac{f_{i+1,j,k} - f_{i,j,k}}{h_i^x} - \frac{f_{i,j,k} - f_{i-1,j,k}}{h_{i-1}^x}\right).$$

Analogous expressions hold in the y and z directions. In this way, the discrete gradient and Laplacian are assembled as

$$\nabla_h f_{i,j,k} = \left(\partial_x f_{i,j,k}, \partial_y f_{i,j,k}, \partial_z f_{i,j,k}\right), \qquad \Delta_h f_{i,j,k} = \partial_{xx} f_{i,j,k} + \partial_{yy} f_{i,j,k} + \partial_{zz} f_{i,j,k}.$$

These formulas are second-order accurate and are exactly the ones we use in the computational implementation.

Fig. 9 presents the reconstruction obtained on a non-uniform mesh. The method is able to recover the location and general shape of the scatterer, and the result remains acceptable. However, the reconstruction quality is somewhat reduced compared to the uniform mesh case, particularly in terms of amplitude accuracy and smoothness of the recovered profile. This difference is expected, since uniform discretizations provide more balanced resolution, whereas non-uniform meshes introduce irregular spacing that can affect the accuracy of finite-difference approximations. Overall, the experiment confirms that the proposed approach remains applicable on non-uniform meshes, though with slightly lower fidelity.

7. Concluding remarks

In this paper, we have developed a comprehensive numerical framework for solving a 3D phaseless coefficient inverse problem governed by the Helmholtz equation. The method is motivated by both practical imaging applications and a longstanding open question in inverse scattering theory concerning the absence of phase information. Our approach combines several key components: a phase retrieval procedure based on the WKB ansatz, a frequency dimension reduction via truncated Fourier expansion, and the application of the Carleman convexification method to stably reconstruct the spatially varying dielectric constant.

Theoretical results guarantee the strict convexity of the proposed cost functional, and the associated gradient descent method is shown to globally converge to the true solution. Through multiple numerical experiments using simulated noisy data, we have demonstrated that the method accurately recovers both the geometry and contrast of embedded scatterers, even in the presence of high noise and under the challenging constraint of single-sided measurements.

Future research directions include extending this framework to other types of governing equations, such as the full Maxwell system, and further reducing data requirements by exploring compressive sensing or machine learning enhancements. Overall, this work offers a globally convergent and computationally feasible solution to a classically ill-posed and practically relevant inverse problem.

CRediT authorship contribution statement

Thuy T. Le: Writing – review & editing, Validation, Software, Methodology, Formal analysis, Data curation; **Phuong M. Nguyen:** Writing – original draft, Software, Methodology, Data curation; **Loc H. Nguyen:** Writing – review & editing, Writing – original draft, Supervision, Software, Project administration, Methodology, Funding acquisition, Formal analysis, Data curation, Conceptualization.

Data availability

Data will be made available on request.

Declaration of competing interest

The author is an Editorial Board Member/Editor-in-Chief/Associate Editor/Guest Editor for this journal and was not involved in the editorial review or the decision to publish this article. The authors declare the following financial interests/personal relationships which may be considered as potential competing interests.

Acknowledgement

The work of P.M.N. and L.H.N. was partially supported by the National Science Foundation under grant DMS-2208159.

References

[1] K. Chadan, P.C. Sabatier, Inverse Problems in Quantum Scattering Theory, Springer, 2nd edition, 1989.
[2] T. Aktosun, P. Sacks, Inverse problem on the line without phase information, Inverse Probl. 14 (1998) 211–224.
[3] M.V. Klibanov, P. Sacks, Phaseless inverse scattering and the phase problem in optics, J. Math. Phys. 33 (1992) 3813–3821.
[4] M.V. Klibanov, On the first solution of a long standing problem: uniqueness of the phaseless quantum inverse scattering problem in 3-D, Appl. Math. Lett. 37 (2014) 82–85.
[5] M.V. Klibanov, Phaseless inverse scattering problems in three dimensions, SIAM J. Appl. Math. 74 (2014) 392–410.
[6] M.V. Klibanov, A phaseless inverse scattering problem for the 3-D Helmholtz equation, Inverse Probl. Imaging 11 (2017) 263–276.
[7] M.V. Klibanov, V.G. Romanov, Uniqueness of a 3-D coefficient inverse scattering problem without the phase information, Inverse Probl. 33 (2017) 95007.
[8] X. Xu, B. Zhang, H. Zhang, Uniqueness in inverse scattering problems with phaseless far-field data at a fixed frequency, SIAM J. Appl. Math. 78 (2018) 1737–1753.
[9] M.V. Klibanov, V.G. Romanov, Explicit formula for the solution of the phaseless inverse scattering problem of imaging of nano structures, J. Inverse Ill-Posed Probl. 23 (2015) 187–193.
[10] M.V. Klibanov, V.G. Romanov, Explicit solution of 3-D inverse scattering problem for the Schrödinger equation: the plane wave case, Eurasian J. Math. Comput. Appl. 3 (2015) 48–63.
[11] M.V. Klibanov, V.G. Romanov, Reconstruction procedures for two inverse scattering problems without the phase information, SIAM J. Appl. Math. 76 (2016) 178–196.
[12] M.V. Klibanov, V.G. Romanov, Two reconsrtuction procedures for a 3-D phaseless inverse scattering problem for the generalized Helmholtz equation, Inverse Probl. 32 (2016) 15005.
[13] M.V. Klibanov, N.A. Koshev, D.-L. Nguyen, L.H. Nguyen, A. Brettin, V.N. Astratov, A numerical method to solve a phaseless coefficient inverse problem from a single measurement of experimental data, SIAM J. Imaging Sci. 11 (2018) 2339–2367.
[14] M.V. Klibanov, D.-L. Nguyen, L.H. Nguyen, A coefficient inverse problem with a single measurement of phaseless scattering data, SIAM J. Appl. Math. 79 (2019) 1–27.
[15] M.V. Klibanov, L.H. Nguyen, K. Pan, Nanostructures imaging via numerical solution of a 3-D inverse scattering problem without the phase information, Appl. Numer. Math. 110 (2016) 190–203.
[16] P. Bardsley, F.G. Vasquez, Imaging with power controlled source pairs, SIAM J. Imaging Sci. 9 (2016) 185–211.
[17] P. Bardsley, F.G. Vasquez, Kirchhoff migration without phases, Inverse Probl. 32 (10) (2016) 105006.
[18] H. Ammari, Y. Chow, J. Zou, Phased and phaseless domain reconstruction in inverse scattering problem via scattering coefficients, SIAM J. Appl. Math. 76 (2016) 1000–1030.
[19] G. Bao, L. Zhang, Shape reconstruction of the multi-scale rough surface from multi-frequency phaseless data, Inverse Probl. 32 (2016) 85002.
[20] O. Ivanyshyn, R. Kress, Inverse scattering for surface impedance from phase-less far field data, J. Comput. Phys. 230 (2011) 3443–3452.
[21] O. Ivanyshyn, R. Kress, P. Serranho, Huygens' principle and iterative methods in inverse obstacle scattering, Adv. Comput. Math. 33 (2010) 413–429.

[22] J. Li, H. Liu, Q. Wang, Enhanced multilevel linear sampling methods for inverse scattering problems, J. Comput. Phys. 257 (2014) 554–571.
[23] Z. Qian, M. Hu, L. Wang, Y. Li, A weighted stabilized Lagrange interpolation collocation method for boundary condition identification in 3D electromagnetic inverse scattering, Adv. Eng. Softw. 197 (2024) 103755.
[24] M. Hu, L. Wang, F. Yang, Y. Zhou, Weighted radial basis collocation method for the nonlinear inverse Helmholtz problems, Mathematics 11 (2023) 662.
[25] V.A. Khoa, G.W. Bidney, M.V. Klibanov, L.H. Nguyen, L. Nguyen, A. Sullivan, V.N. Astratov, Convexification and experimental data for a 3D inverse scattering problem with the moving point source, Inverse Probl. 36 (2020) 85007.
[26] V.A. Khoa, M.V. Klibanov, L.H. Nguyen, Convexification for a 3D inverse scattering problem with the moving point source, SIAM J. Imaging Sci. 13 (2) (2020) 871–904.
[27] T.T. Le, L.H. Nguyen, The gradient descent method for the convexification to solve boundary value problems of quasi-linear PDEs and a coefficient inverse problem, J. Sci. Comput. 91 (3) (2022) 74.
[28] P.N.H. Le, T.T. Le, L.H. Nguyen, The Carleman convexification method for Hamilton-Jacobi equations Comput. Math. Appl. 159 (2024) 173–185.
[29] C.L. Critchfield, The WKB method in three dimensions, Am. J. Phys. 32 (1964) 597.
[30] C.E. Hecht, J.E. Mayer, Extension of the WKB equation, Phys. Rev. 106 (1957) 1156.
[31] S.C. Miller, R.H. Good, A WKB-type approximation to the Schrödinger equation, Phys. Rev. 91 (1953) 174.
[32] B.R. Vainberg, On the short wave asymptotic behaviour of solutions of stationary problems and the asymptotic behaviour as $t \to \infty$ of solutions of non-stationary problems, Russ. Math. Surv. 30 (2) (1975) 1–58.
[33] D. Colton, R. Kress, Inverse acoustic and electromagnetic scattering theory, in: Applied Mathematical Sciences, New York, Springer, 2013. 3rd edition.
[34] V.A. Khoa, G.W. Bidney, M.V. Klibanov, L.H. Nguyen, L. Nguyen, A. Sullivan, V.N. Astratov, An inverse problem of a simultaneous reconstruction of the dielectric constant and conductivity from experimental backscattering data, Inverse Probl. Sci. Eng. 29 (5) (2021) 712–735.
[35] P.M. Nguyen, L.H. Nguyen, H.T. Vu, A Global Approach for the Inverse Scattering Problem Using a Carleman Contraction Map, Technical Report, preprint, 2024.
[36] T.T. Le, L.H. Nguyen, A convergent numerical method to recover the initial condition of nonlinear parabolic equations from lateral Cauchy data, J. Inverse Ill-Posed Probl. 30 (2) (2022) 265–286.
[37] L.H. Nguyen, The Carleman contraction mapping method for quasilinear elliptic equations with over-determined boundary data, Acta Math. Vietnam. 48 (2023) 401–422.
[38] M.V. Klibanov, D.-L. Nguyen, L.H. Nguyen, H. Liu, A globally convergent numerical method for a 3D coefficient inverse problem with a single measurement of multi-frequency data, Inverse Probl. Imaging 12 (2018) 493–523.
[39] M.V. Klibanov, Convexification of restricted Dirichlet to Neumann map, J. Inverse Ill-Posed Probl. 25 (5) (2017) 669–685.
[40] P.M. Nguyen, T.T. Le, L.H. Nguyen, M.V. Klibanov, Numerical differentiation by the polynomial-exponential basis, J. Appl. Ind. Math. 17 (2023) 928–942.
[41] M.V. Klibanov, O.V. Ioussoupova, Uniform strict convexity of a cost functional for three-dimensional inverse scattering problem, SIAM J. Math. Anal. 26 (1995) 147–179.
[42] M.V. Klibanov, Z. Li, W. Zhang, Convexification for the inversion of a time dependent wave front in a heterogeneous medium, SIAM J. Appl. Math. 79 (2019) 1722–1747.
[43] L.H. Nguyen, Q. Li, M.V. Klibanov, A convergent numerical method for a multi-frequency inverse source problem in inhomogenous media, Inverse Probl. Imaging 13 (2019) 1067–1094.
[44] A.B. Bakushinskii, M.V. Klibanov, N.A. Koshev, Carleman weight functions for a globally convergent numerical method for ill-posed Cauchy problems for some quasilinear PDEs, Nonlinear Anal. Real World Appl. 34 (2017) 201–224.
[45] A. Lechleiter, D.-L. Nguyen, A trigonometric Galerkin method for volume integral equations arising in TM grating scattering, Adv. Comput. Math. 40 (2014) 1–25.
[46] D.L. Nguyen, A volume integral equation method for periodic scattering problems for anisotropic Maxwell's equations, Appl. Numer. Math. 98 (2015) 59–78.